JACS
JOURNAL OF THE AMERICAN CHEMICAL SOCIETY

ARTICLE

pubs.acs.org/JACS

Theoretical Study on the Mechanism of the Oxygen Activation Process in Cysteine Dioxygenase Enzymes

Devesh Kumar,*[,†,‡] Walter Thiel,[†] and Sam P. de Visser*[,§]

[†]Max-Planck-Institut für Kohlenforschung, Kaiser-Wilhelm-Platz 1, D-45470 Mülheim an der Ruhr, Germany

[‡]Molecular Modelling Group, Indian Institute of Chemical Technology, Hyderabad 500 607, India

[§]The Manchester Interdisciplinary Biocenter and School of Chemical Engineering and Analytical Science, University of Manchester, 131 Princess Street, Manchester M1 7DN, United Kingdom

Supporting Information

ABSTRACT: Cysteine dioxygenase (CDO) is a vital enzyme for human health involved in the biodegradation of toxic cysteine and thereby regulation of the cysteine concentration in the body. The enzyme belongs to the group of nonheme iron dioxygenases and utilizes molecular oxygen to transfer two oxygen atoms to cysteinate to form cysteine sulfinic acid products. The mechanism for this reaction is currently disputed, with crystallographic studies implicating a persulfenate intermediate in the catalytic cycle. To resolve the dispute we have performed quantum mechanics/molecular mechanics (QM/MM) calculations on substrate activation by CDO enzymes using an enzyme monomer and a large QM active region. We find a stepwise mechanism, whereby the distal oxygen atom of the iron(II)-superoxo complex attacks the sulfur atom of cysteinate to form a ring structure, followed by dioxygen bond breaking and the formation of a sulfoxide bound to an iron(IV)-oxo complex. A sulfoxide rotation precedes the second oxygen atom transfer to the substrate to give cysteine sulfinic acid products. The reaction takes place on several low-lying spin-state surfaces via multistate reactivity patterns. It starts in the singlet ground state of the iron(II)-superoxo reactant and then proceeds mainly on the quintet and triplet surfaces. The initial and rate-determining attack of the superoxo group on the cysteinate sulfur atom involves a spin-state crossing from singlet to quintet. We have also investigated an alternative mechanism via a persulfenate intermediate, with a realignment of hydrogen bonding interactions in the substrate binding pocket. However, this alternative mechanism of proximal oxygen atom attack on the sulfur atom of cysteinate is computed to be a high-energy pathway, and therefore, the persulfenate intermediate is unlikely to participate in the catalytic cycle of CDO enzymes.

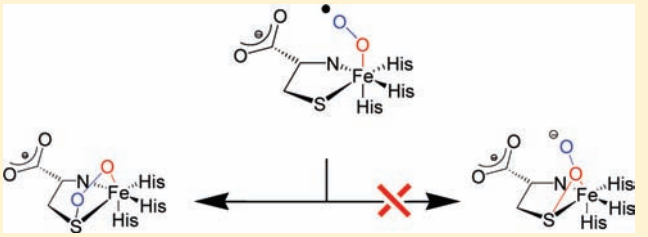

I. INTRODUCTION

Mononuclear nonheme iron-containing enzymes are common enzymes in the body involved in key biochemical processes for human health. Because of their large versatility of substrate activation they are implicated with a broad range of catalytic functions.[1] A large group of these mononuclear nonheme iron containing enzymes utilize α-ketoglutarate as a cosubstrate and act as dioxygenases (α-ketoglutarate-dependent dioxygenases)[2] with biochemical functions that, e.g., include DNA and RNA base repair, molecular responses to hypoxia, and oxygen sensing.[3,4] Generally, these enzymes bind α-ketoglutarate to an iron(II) center that is linked to the protein backbone via a 2His/1Asp facial triad ligand motif,[5] while substrate binds in the vicinity. Dioxygen binding to the iron center typically leads to decarboxylation of α-ketoglutarate to form succinate and an iron(IV)-oxo species that is the active oxidant of substrate hydroxylation reactions.[6] High-valent iron(IV)-oxo complexes have been identified as the active oxidant of many heme and nonheme mono- and dioxygenases and are known to efficiently abstract hydrogen atoms from aliphatic substrates.[1,7] The iron(IV)-oxo active species of two α-ketoglutarate dependent dioxygenases, namely, taurine/α-ketoglutarate dioxygenase (TauD) and prolyl-4-hydroxylase, have been trapped and characterized by resonance Raman, Mössbauer, and extended X-ray absorption fine structure (EXAFS) studies.[8]

Despite the fact that most mononuclear nonheme iron dioxygenases have a 2His/1Asp structural motif, there are several dioxygenases with different ligand binding motifs.[9] For example, acetylacetone Dke1 contains a transition metal active site where three histidine groups bind to the metal,[10] while in quercetin dioxygenase the metal is bound to the side chains of three histidine and one glutamic acid group via a 3His/1Glu structural motif.[11] Another mononuclear nonheme iron dioxygenase with a 3His metal binding motif is cysteine dioxygenase (CDO), which is a vital enzyme for human health involved in the metabolism of toxic cysteine in the body (Scheme 1).[12] Thus, a decline in CDO

Received: August 19, 2010
Published: February 23, 2011

dx.doi.org/10.1021/ja107514f | J. Am. Chem. Soc. 2011, 133, 3869–3882

Scheme 1. Reaction Catalyzed by CDO Enzymes

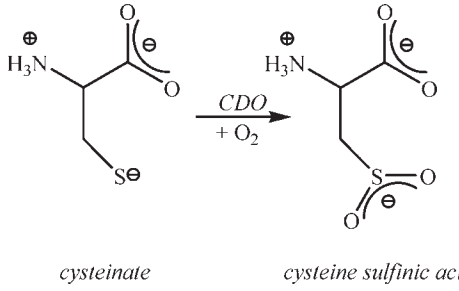

activity has been associated with neurological disorders,[13] including diseases such as Alzheimer's and Parkinson's.[14] Because of its importance for human health, many studies have been reported on the catalytic mechanism of cysteine dioxygenation by CDO enzymes.[15,16]

There are various enzymes in nature apart from CDO that catalyze *S*-oxygenation reactions, including heme enzymes, such as the cytochromes P450[7,17] and the nonheme iron enzyme nitrile hydratase.[18] The nitrile hydratases contain a cysteinate group ligated to the metal, which has been shown to be oxygenated in the reaction mechanism.[19] This discovery led to the synthesis and study of many biomimetic complexes containing an iron ligated to a thiolate group.[20] Indeed some of these complexes react with dioxygen to form oxygenated metal−ligands. Recently, a biomimetic model of CDO was created, which also reacted with molecular oxygen via a metal−ligand *S*-oxygenation.[21]

Figure 1 displays an extract of the active site of CDO as taken from the 2IC1 protein databank (pdb) file.[22] The metal is linked to three imidazole groups of His_{86}, His_{88}, and His_{140} that form a facial triad typical for nonheme iron dioxygenases. Substrate cysteinate binds as a bidentate ligand through the thiolate and amine groups that are located trans to the His_{140} and His_{88} ligands, respectively. The last binding site of iron is vacant in Figure 1 but is reserved for molecular oxygen. The carboxylic acid group of substrate cysteinate forms a salt bridge with the methylguanidinium group of Arg_{60}. Further hydrogen-bonding interactions that stabilize this salt bridge come from the phenol group of Tyr_{157} and the imidazole group of His_{155}. An interesting feature of the active site of CDO is the covalent linkage between the thiolate side chain of Cys_{93} with the aromatic ring of Tyr_{157}. It has been hypothesized[23] that substrate binding to the active center leads to the formation of this Cys_{93}−Tyr_{157} linkage. Site-directed mutations showed that this linkage improved the catalytic efficiency 10-fold but it is not clear how.[12b]

To gain insight into dioxygen activation by nonheme iron containing enzymes and their ligand systems, we performed a series of density functional theory (DFT) studies on TauD as well as on CDO enzymes.[16,24] These studies were focused on the oxygen activation mechanism for CDO and three of its active-site mutants, whereby one of the His ligands was replaced by a carboxylic acid group. The calculations highlighted the importance of the 3His ligand system in CDO enzymes to accommodate optimal substrate dioxygenation. Calculations on CDO mutants with a 2His/1Asp structural ligand system gave increased reaction barriers and in some cases a mechanism that stops after one oxygen atom is transferred.[16b] Our DFT study on the active site of CDO enzymes established a possible

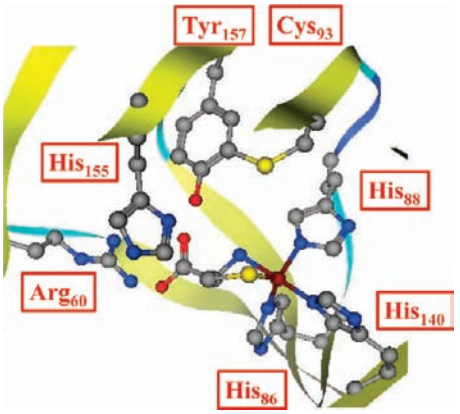

Figure 1. Active-site structure of CDO enzymes as taken from the 2IC1 pdb file.[22] All amino acids are labeled as in the corresponding pdb file.

mechanism of the oxygen activation process (mechanism I in Scheme 2).[16] It was proposed that the dioxygen molecule binds in an end-on fashion (**A**) and that the dioxygen activation process starts with attack of the distal oxygen atom (O_d) on the sulfur of the cysteinate side chain via a barrier $\mathbf{TS_A}$ to form a ring structure with an S−Fe−O−O four-membered ring (**B**). A subsequent dioxygen bond breakage via a barrier $\mathbf{TS_B}$ then leads to cysteine oxide and an iron(IV)-oxo species (**C**). The sulfoxide group undergoes an internal rotation via a barrier $\mathbf{TS_C}$ to make space for the second incoming oxygen atom (Structure **C′**). A fast rebound reaction via barrier $\mathbf{TS_D}$ leads to cysteine sulfinic acid products (**D**). DFT studies established that the rate-determining step in this process is the barrier via $\mathbf{TS_A}$ and that a conversion from a ground state singlet spin state to a quintet spin state precedes the barrier leading to the ring structure.[16]

This DFT-based mechanism was disputed by experimental X-ray studies on a CDO enzyme that detected a persulfenate intermediate.[25] These experimental studies were unable to resolve whether the persulfenate is an intermediate in the catalytic cycle or a dead-end product from a side reaction. However, an alternative mechanism was suggested (mechanism II in Scheme 2),[25] whereby a hydrogen bonding interaction of the phenol group of Tyr_{157} with the distal oxygen atom of the O_2 group in structure **A** facilitates the dioxygenation mechanism through an initial S−O bond formation between the cysteine sulfur atom and the proximal oxygen atom (O_p) to form the persulfenate intermediate (structure **E**). Subsequently, the distal oxygen atom forms a bond with sulfur to form a ring-structure **F** after which the dioxygen bond breaks to form a sulfoxide intermediate (**G**). A final oxygen atom transfer then gives cysteine sulfinic acid products.

Clearly, the mechanism of CDO enzymes is unresolved and surrounded by controversies that call for further studies, especially with regard to the impact of the protein environment on the mechanism and on the possible involvement of persulfenate intermediates. Since the earlier computational work had addressed only small gas-phase model systems and mechanism I, we decided to reinvestigate cysteine dioxygenation in CDO enzymes by performing quantum mechanics/molecular mechanics (QM/MM) calculations[26] on a realistic model of the full enzyme for both proposed mechanisms. Previous DFT and QM/MM studies on the enzyme cytochrome P450 have revealed differences in the mechanism and the electronic configuration of active oxidants when the protein environment is taken into account at the QM/MM level.[27] Moreover, Lundberg

Scheme 2. Suggested Mechanisms of Cysteine Metabolism by CDO Enzymes As Taken from Refs 16 and 23

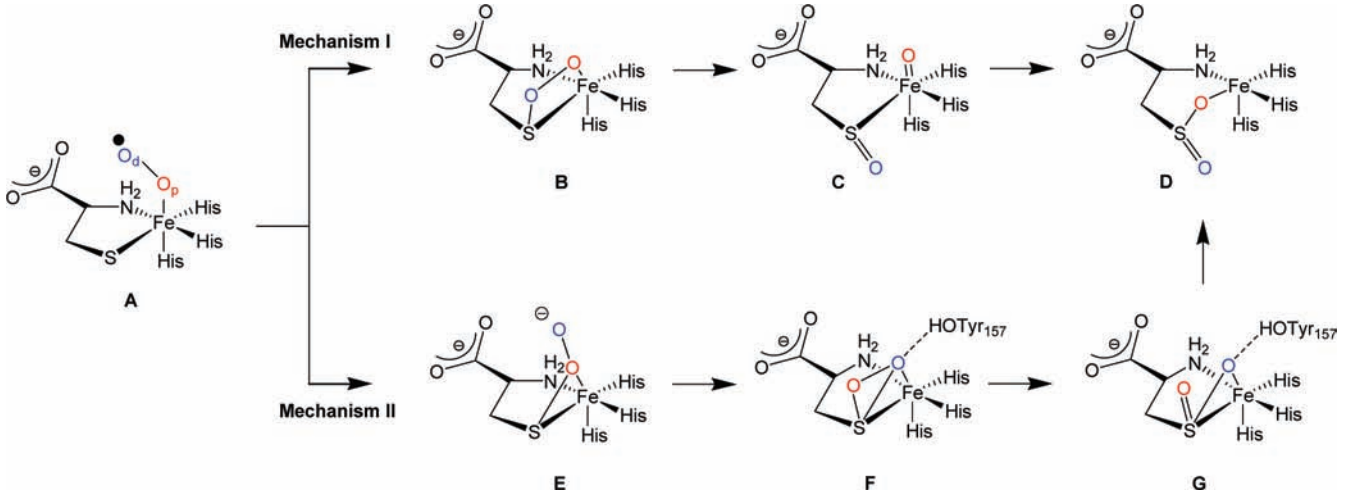

and Morokuma have shown in the case of isopenicillin *N* synthase that a QM/MM treatment is required for the dioxygen binding step in the catalytic cycle, since small model complexes failed to describe this step correctly.[28] In this work, we present the first QM/MM study on the oxygen activation mechanism in CDO enzymes via mechanisms I and II. The QM/MM calculations confirm the dioxygen activation mechanism proposed on the basis of DFT model calculations and assign the persulfenate structure as an intermediate of a side reaction. These findings may also be relevant for other dioxygenases.

II. COMPUTATIONAL METHODS

A. Setup of the System. Our calculations use methods and procedures previously applied in QM/MM studies of the cytochromes P450 and TauD enzymes.[29,30] The initial coordinates were taken from the pdb file 2IC1, which represents a substrate-bound CDO monomer.[22] Hydrogen atoms were added as well as an O_2 molecule to create an iron(II)-superoxo bound intermediate in the catalytic cycle of CDO. Solvation and protonation schemes were applied in an analogous manner as before.[27a,31] Briefly, the protonation states of most residues were determined from the pK_a values calculated with the PropKa program, except for the histidine side chains whose protonation states were assigned by visual inspection of their local environment as follows: His_{20}, His_{81}, His_{82}, His_{92}, His_{165}, and His_{173} were protonated at the NE atom and His_{86}, His_{88}, His_{140}, and His_{155} at the ND atom. The overall system was charge neutral and consisted of 24,779 atoms including 7,109 TIP3P water molecules. CDO was solvated in a pre-equilibrated water sphere of 40 Å and the solvated system was energy minimized followed by a molecular dynamics (MD) simulation at the MM level using the CHARMM22 force field[32] as implemented in the CHARMM program package.[33] The Fe atom, the dioxygen group, the cysteinate substrate, and the His_{86}, His_{88}, and His_{140} residues as well as the outer 8 Å of solvent layer were kept fixed during the classical energy minimizations and MD simulations. Energy-minimized snapshots from the MD trajectories were taken as starting structures for the QM/MM calculations. The CHARMM22 force field[32] served as MM component in all QM/MM calculations.

B. QM/MM Geometry Optimizations. The active region in QM/MM geometry optimizations comprised the QM region (see below) and all residues and water molecules within an 8 Å distance from Fe or any other active-site atom (dioxygen, His_{86}, His_{88}, His_{140}, or cysteinate substrate). Consequently, close to 1,500 atoms in the MM region were fully optimized in the individual snapshots during the QM/MM calculations, while the remaining MM atoms were fixed.

Transition-state structures were located as follows: Initially detailed geometry scans between the two local minima were performed in either direction. The maxima of these geometry scans were used as starting points of full transition state optimizations. Numerical frequency calculations were done at the QM/MM level to characterize the optimized structures as transition states with one imaginary frequency for the correct mode. Extensive geometry scans from reactants to products and vice versa on the singlet, triplet, and quintet spin states confirmed the proposed reaction mechanisms by establishing contiguous paths between the stationary points.

C. QM Part of the QM/MM Calculations. Following previous experience in the field,[34−36] our default QM treatment employed unrestricted hybrid density functional theory (UB3LYP)[37,38] in combination with a Los Alamos-type LACVP basis set on Fe (with a small core ECP) and 6-31G on the other atoms: basis set B1.[39] Full geometry optimizations were normally done with basis set B1 (unless otherwise noted). Subsequent single-point calculations on the optimized geometries made use of the Wachters all-electron basis set on iron and 6-31+G* on the remaining atoms in the QM region, basis set B2W.[40] To ascertain that our default level is sufficient, we performed additional geometry optimizations on **A**, $\mathbf{TS_A}$, and **B** (Scheme 2) using B3LYP/CHARMM in combination with a larger TZVP basis set,[41] which gave only slightly different results (see section III.A) and thus supported our choice of basis set B1 for geometry optimizations.

In our previous work on cytochrome P450 enzymes, the QM approach outlined above was found to reproduce experimental free energies of activation for aliphatic hydroxylation and epoxidation reactions within 3 kcal mol^{-1}.[34a,34b] Moreover, the errors in the barriers were systematic so that the relative values for a series of aliphatic hydroxylation reactions were accurate to within 1 kcal mol^{-1}.[34c,34d] Benchmark calculations for kinetic isotope effects[35] and spectroscopic (vibrational as well as electron paramagnetic resonance (EPR)) parameters[36] also reproduced the available experimental data very well. For further validation in the present CDO system, we tested the effect of the chosen density functional on the ordering and relative energies of the lowest-lying spin states in the iron(II)-superoxo complex by running single-point calculations using the BLYP,[38,42] BP86,[42,43] PBE0,[44] OLYP,[38,45] and OPBE[45,46] functionals with basis set B1 on the UB3LYP/B1 optimized geometries. Since the latter two density

dx.doi.org/10.1021/ja107514f |*J. Am. Chem. Soc.* 2011, 133, 3869–3882

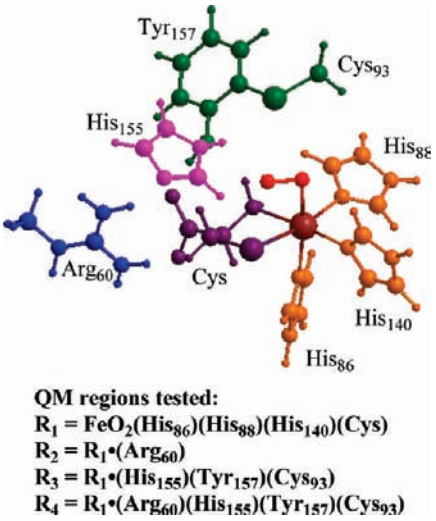

Figure 2. Definition of the four QM regions (R_1, R_2, R_3, and R_4) tested in the calculations.

functionals have not been implemented in TURBOMOLE yet, these calculations were done at the QM level using Gaussian 09.[47] In addition, we ran single-point calculations using a dispersion-corrected B3LYP method (B3LYP-D).[48]

The complete project generated a considerable amount of data (spin densities, charge distributions, detailed geometries, potential energy scans, etc.), which are documented in the Supporting Information that accompanies this paper.

An electronic embedding scheme[49] was adopted in the QM/MM calculations, whereby the interactions of the electrons in the QM region with charges in the MM region are incorporated into the one-electron Hamiltonian of the QM calculation. No cutoffs were introduced for the nonbonding MM and QM/MM interactions. The QM/MM boundary was treated with hydrogen link atoms through the charge shift model. The TURBOMOLE program package[50] was used for the QM treatment in the QM/MM as well as in the pure QM calculations. The CHARMM-22 force field was run through the DL_POLY[51] program to handle the MM part of the systems. The QM/MM calculations were performed with the ChemShell package[52] that integrates the TURBOMOLE and DL_POLY programs and performs geometry optimizations with the HDLC optimizer.[53]

D. Snapshots. Seven different snapshots were selected from an initial classical MD simulation after 0, 50, 100, 150, 200, 250, and 2000 ps and subjected to combined QM/MM calculations (full system).

E. QM Regions. We employed four different QM regions: R_1, R_2, R_3, and R_4, as defined in Figure 2. The smallest QM region, R_1, contains the metal, dioxygen, substrate cysteinate (Cys), and imidazole groups replacing the three histidine ligands. To test the effect of secondary sphere amino acids on the substrate dioxygenation mechanism, we enlarged the QM region with the methylguanidinium group of Arg_{60} in R_2, which also changes the total charge of the QM region from neutral to +1. QM region R_3, which is overall neutral in charge, consists of R_1 plus the phenol group of Tyr_{157}, its covalently linked Cys_{93} as methylsulfide and another imidazole group for His_{155}. Our largest QM region, R_4, contains R_1 and the amino acid side chains of Arg_{60}, His_{155}, Tyr_{157}, and Cys_{93} to account for the effects of all secondary amino acids. Consequently, QM region R_4 is also singly positively charged.

R_1 (42 atoms): Fe, O1, O2, Cys_{202}, His_{86}, His_{88}, His_{140}
R_2 (55 atoms): R_1, Arg_{60}
R_3 (68 atoms): R_1, His_{155}, Tyr_{157}, Cys_{93}
R_4 (81 atoms): R_1, Arg_{60}, His_{155}, Tyr_{157}, Cys_{93}

III. RESULTS

A. Benchmark Studies on Accuracy and Reproducibility of the Methods. Recent work of Lundberg and Morokuma on dioxygen binding to an iron center of the enzyme isopenicillin *N*-synthase showed that DFT calculations on small enzyme models can give rise to large systematic errors due to the fact that the interactions of the protein environment with the active center are not taken into consideration.[28] This is particularly essential for dioxygen binding processes, and therefore, QM/MM studies should give more reliable structures and energetics than those obtained with small DFT models. Consequently, we decided to investigate the catalytic mechanism of CDO enzymes using QM/MM techniques. Unfortunately, it is impossible to calibrate our calculations on CDO catalytic cycle intermediates against experiment due to the absence of spectroscopic data on dioxygen bound intermediates. Thus, we started our work with an extensive set of calibration calculations on the reactant, namely, the Fe(II)-superoxo bound complex of CDO. Specifically, we tested the reproducibility of the calculations by using a selection of different MD snapshots, QM regions, density functionals, and basis sets.

First, we computed the iron(II)-superoxo complex (**A**) in the lowest-lying singlet, triplet, and quintet spin states using seven different snapshots (Sn) from the MD simulations taken after 0, 50, 100, 150, 200, 250, and 2000 ps. These values are given in subscript to the snapshot label; for example, Sn_{100} denotes calculations starting from the snapshot taken after 100 ps. Figure 3 gives the ordering and relative energies of the lowest-lying spin states for these snapshots. Note that all optimized geometries of structure **A** refer to an end-on bound iron(II)-superoxo group. We made efforts to find a side-on bound structure which, however, did not succeed since the geometry optimizations always converged to end-on bound structures instead. In all cases, the singlet spin state is the ground state followed by the triplet and quintet spin states, respectively. These spin state orderings are in agreement with previous studies on iron(II)-superoxo complexes in taurine/α-ketoglutarate dioxygenase[24c] and cytochrome P450 enzymes.[54] The iron(II)-superoxo intermediate in the catalytic cycle of cytochrome P450 is known to have a singlet ground state, both computationally and experimentally (EPR).[54] Recent biomimetic studies on iron(II)-superoxo and iron(III)-peroxo complexes in porphyrin-ligated complexes showed a delicate balance between the two configurations.[55] Apparently, the local environment of the dioxygen moiety in CDO stabilizes the iron(II)-superoxo over the iron(III)-peroxo species.

The average value and standard deviation of the singlet−triplet energy gaps (ΔE_{ST}) of these snapshots are $\Delta E_{ST} = 4.0 \pm 0.6$ kcal mol^{-1} for the B1 data and $\Delta E_{ST} = 4.3 \pm 0.7$ kcal mol^{-1} for the B2W results. Therefore, within the error bars of the calculations, both basis sets give the same singlet−triplet energy gap. The singlet−quintet energy gap (ΔE_{SQ}), by contrast, shows somewhat larger fluctuations among the snapshots, covering a range of about 4.0 kcal mol^{-1} for each basis set, with an average value and standard deviation of $\Delta E_{SQ} = 10.8 \pm 1.6$ kcal mol^{-1} for basis set B1 and $\Delta E_{SQ} = 13.9 \pm 1.7$ kcal mol^{-1} for B2W. Hence, enlarging the basis set from B1 to B2W has only minor effects on the computed singlet−triplet energy gaps, whereas the singlet−quintet energy gaps are more sensitive and generally increase slightly upon basis set extension. Since all snapshots predict the same trends and spin state ordering, we decided to perform the

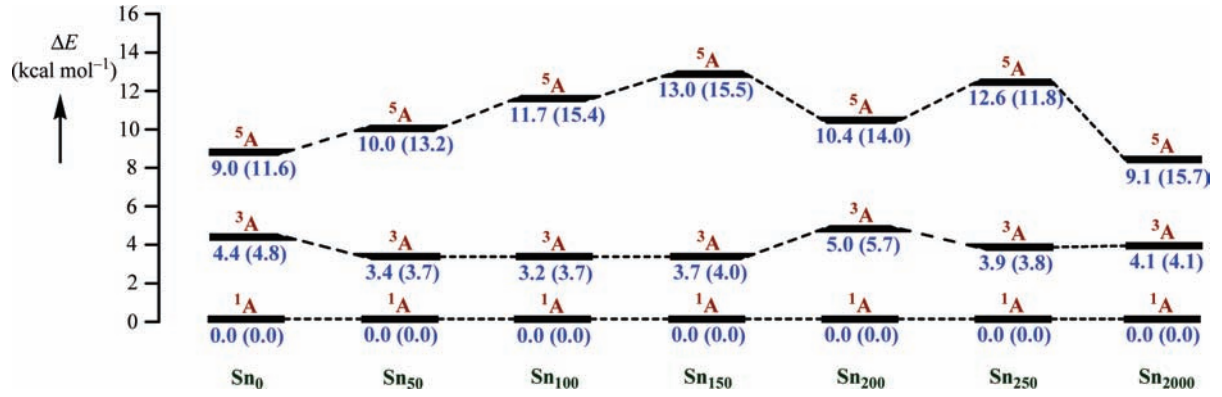

Figure 3. Relative energies (in kcal mol^{-1}) of the lowest-lying singlet, triplet, and quintet spin states of the iron(II)-superoxo complex (^{1,3,5}**A**) of CDO as calculated using seven different snapshots from the MD simulations and QM region R_4. All data were obtained with QM/MM using B3LYP/B1 optimizations and QM region R_4. Values in parentheses were calculated at the B3LYP/B2W//B3LYP/B1 level of theory.

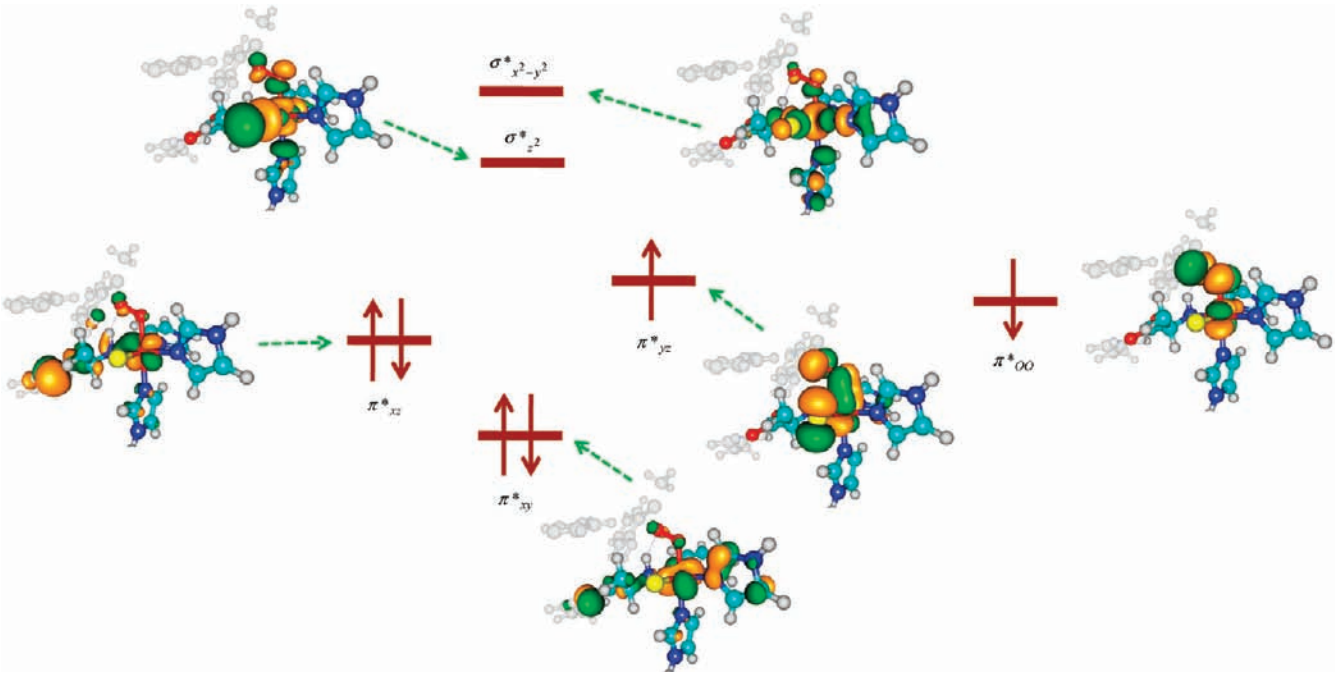

Figure 4. High-lying occupied and low-lying virtual molecular orbitals of ^{1}**A**.

dioxygen activation studies using two different snapshots only, namely, Sn_{100} and Sn_{200}, which are expected to provide a good representation of the actual system.

The DFT calculations on the iron(II)-superoxo complex ^{1,3,5}**A** from ref 16 are in good agreement with the QM/MM calculations presented here. They gave a singlet spin ground state with the triplet and quintet spin states higher in energy by ΔE_{ST} = 2.6 kcal mol^{-1} and ΔE_{SQ} = 5.9 kcal mol^{-1} at the B3LYP/B2//B3LYP/B1 level of theory, where B2 denotes an LACV3P+ basis set on iron and 6-311+G* on the other atoms. Inclusion of a dielectric continuum with ε = 5.7 in the DFT treatment raised ΔE_{SQ} to 8.4 kcal mol^{-1}, while a ΔE_{ST} was only marginally influenced (ΔE_{ST} = 2.0 kcal mol^{-1}).[16b] The previous DFT calculations give the same spin-state ordering as the present QM/MM results and are consistent with a small singlet−triplet energy gap of about 2−4 kcal mol^{-1}. The effect of the protein on the spin-state ordering and relative energies of the iron(II)-superoxo complex is thus rather small.

To understand the electronic differences between the various spin states, consider first the high-lying occupied and low-lying virtual orbitals of our reactant complex ^{1}**A** in Figure 4. The orbitals are dominated by metal 3d contributions. The lowest one depicted in Figure 4 is the doubly occupied π^*_{xy} orbital, a nonbonding orbital in the plane of the cysteinate ligand. Somewhat higher in energy is the doubly occupied π^*_{xz} orbital, which is parallel to the O−O bond and shows little interaction with the dioxygen moiety. There are two singly occupied orbitals in ^{1}**A** and ^{3}**A**, namely, the π^*_{yz} and π^*_{OO} orbitals. The former represents an antibonding interaction between the metal $3d_{yz}$ and a 3p orbital on sulfur and also interacts with the dioxygen group, while the latter is antibonding along the dioxygen bond. Finally, the virtual $\sigma^*_{z^2}$ orbital represents the antibonding combination of $3d_{z^2}$ on iron with distal and axial ligands as well as with a σ-orbital on sulfur, whereas the virtual $\sigma^*_{x^2-y^2}$ orbital involves interactions between iron $3d_{x^2-y^2}$ and orbitals on histidine and substrate amide groups. The orbitals shown in

dx.doi.org/10.1021/ja107514f |J. Am. Chem. Soc. 2011, 133, 3869–3882

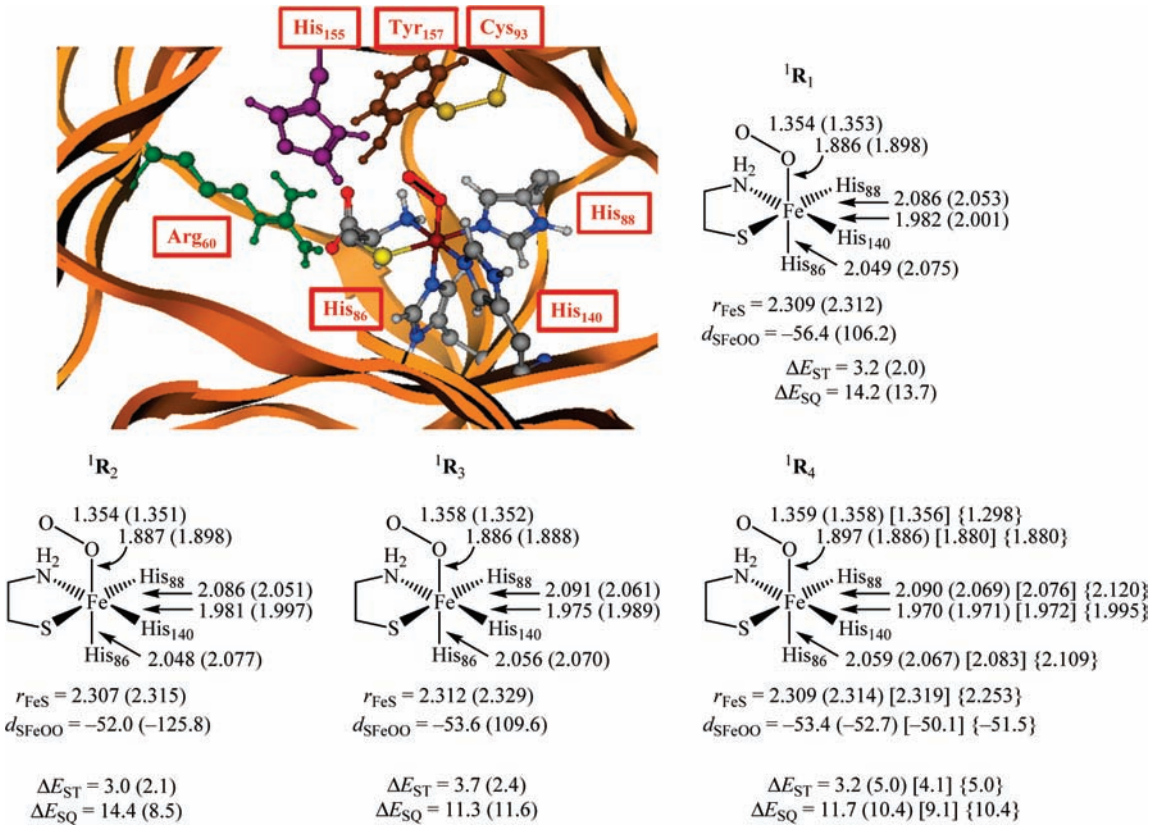

Figure 5. Optimized geometries of the singlet spin iron(II)-superoxo bound species (^{1}**A**) using different size QM regions (R_1, R_2, R_3, and R_4 as defined in Figure 2). Only the metal and its ligands are shown. All bond lengths are given in angstroms and the dihedral angle S−Fe−O−O (d_{SFeOO}) is given in degrees. Optimized geometries are obtained from snapshot Sn_{100} (Sn_{200}) [Sn_{2000}] {Sn_{200}-TZVP}. Relative energies (in kcal mol^{-1}) are based on the B1 results.

Figure 4 are occupied with six electrons and give an orbital occupation of $\pi^*_{xy}{}^2\,\pi^*_{xz}{}^2\,\pi^*_{yz}{}^1\,\pi^*_{OO}{}^1$ for ^{1}**A** as assigned with the arrows next to the orbitals. The triplet spin state (^{3}**A**) has the same orbital occupation as the singlet spin state, but the unpaired electrons are ferromagnetically rather than antiferromagnetically coupled. As a consequence, ^{3}**A** and ^{1}**A** are close in energy, with an average energy gap of 4.3 kcal mol^{-1} (B3LYP/B2W) for seven different MD snapshots (vide supra). The singlet and triplet spin states have the same orbital occupation in the present QM/MM and the previous DFT model calculations, and they can both be characterized as an iron(II)-superoxo complex. In ^{5}**A** the system is also described as a iron(II)-superoxo complex, but with orbital occupation $\pi^*_{xy}{}^2\,\pi^*_{xz}{}^1\,\pi^*_{yz}{}^1\,\sigma^*_{z^2}{}^1\,\pi^*_{OO}{}^1$.

As already shown by DFT model calculations,[16] the ^{5}**A** state is an excited state of the iron(II)-superoxo complex of CDO. Its energy relative to the singlet spin ground state (ΔE_{SQ}) is influenced by the protein environment, as indicated by the fluctuations in the computed singlet−quintet energy gaps for our seven QM/MM snapshots (vide supra). Electronically, in four of the seven snapshots, the ^{5}**A** state has group spin densities of $\rho_{Fe} = 3.72-3.76$, $\rho_{OO} = 0.42-0.56$, and $\rho_{Cys} = -0.31$ through -0.46 (B3LYP/B2W), which are similar to the DFT values obtained for the small model complex. These group spin densities reflect a dominant $\pi^*_{xy}{}^2\,\pi^*_{xz}{}^1\,\pi^*_{yz}{}^1\,\sigma^*_{z^2}{}^1\,\pi^*_{OO}{}^1$ configuration.[16] A natural orbital analysis of the QM/MM wave function shows some admixture of the $\pi^*_{xy}{}^2\,\pi^*_{xz}{}^1\,\pi^*_{yz}{}^1\,\sigma^*_{z^2}{}^1\,\sigma^*_{x^2-y^2}{}^1\,lp_S{}^1\,\pi^*_{OO}{}^1$ configuration, which is due to an electron transfer from a lone pair on the sulfur of cysteinate (lp_S orbital) into a virtual metal-based orbital ($\sigma^*_{x^2-y^2}$) with σ-type antibonding interactions along the Fe−S bond. As a consequence, the spin densities on the metal and the cysteinate ligand are somewhat larger than expected. Attempts to swap orbitals and create a configurationally more pure quintet state failed and converged back to this mixed state. Two of the seven snapshots give different group spin densities (B3LYP/B2W) with $\rho_{Fe} = 2.82$ or 2.84, $\rho_{OO} = 0.80$ or 0.79, and $\rho_{Cys} = 0.31$ or 0.30 for Sn_{150} and Sn_{250}, respectively. Attempts to swap orbitals in these two cases failed to converge to the type of quintet state found for the other snapshots and DFT model complexes. Energetically, there is no significant difference between the quintet state energies (ΔE_{SQ}) obtained for snapshots Sn_{150} and Sn_{250} as compared to the other snapshots. It thus seems that environmental perturbations affect the exact nature of the quintet spin state and may lead to a different mix of energetically close-lying configurations in the quintet spin-state wave function.

Subsequently, we tested the effect of the size of the QM region on the spin-state ordering, optimized geometries, and relative energies. Thus, we investigated two characteristic snapshots (Sn_{100} and Sn_{200}) and ran full geometry optimizations using four different QM regions (R_1, R_2, R_3, and R_4) as defined above in Figure 2. This was done to establish the effect of second sphere coordination atoms on the optimized geometries and the charge distributions. Additionally, we performed two more geometry optimizations on QM region R_4: one after a long 2000-ps MD run (Sn_{2000}) and one on Sn_{200} using the B3LYP/TZVP method for the QM region (Sn_{200}-TZVP). Figure 5 shows the optimized

dx.doi.org/10.1021/ja107514f |J. Am. Chem. Soc. 2011, 133, 3869–3882

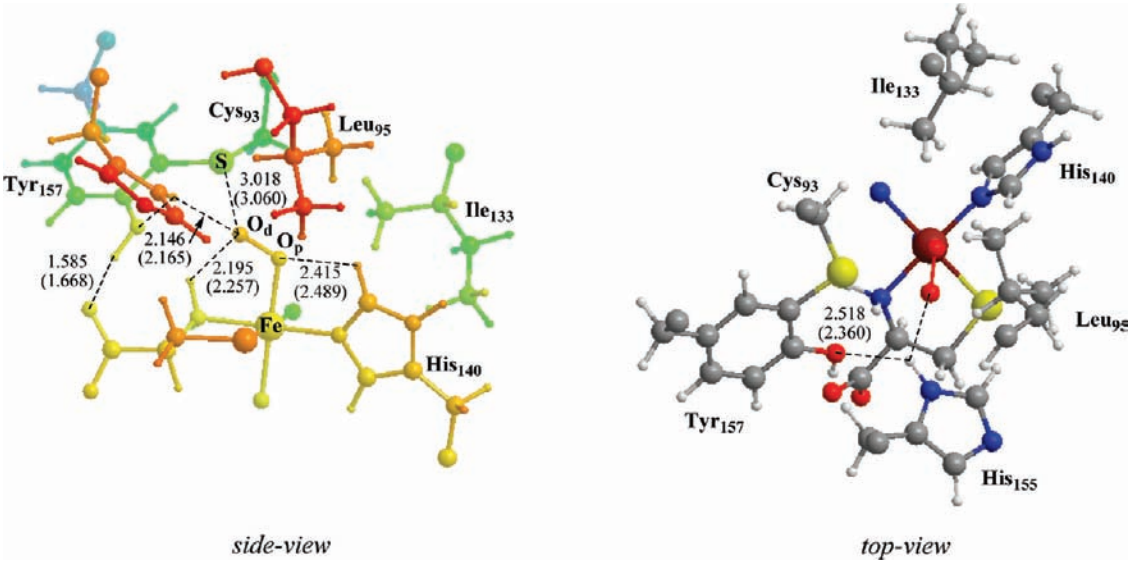

Figure 6. Extracts of optimized geometries, with focus on the dioxygen environment of ^{1}**A**, from QM(B3LYP/B1)/CHARMM and QM(B3LYP/TZVP)/CHARMM (data in parentheses). Bond lengths are given in angstroms. Calculations were done with QM region R_4, but only selected QM and MM atoms are shown.

geometries in the singlet spin ground state as well as the adiabatic excitation energy from the singlet to the lowest-lying triplet (ΔE_{ST}) and quintet (ΔE_{SQ}) spin states, respectively. Generally the optimized bond lengths (UB3LYP/B1) are very similar for the four QM regions (typically within 0.010 Å, maximum deviation of 0.030 Å). The same is true for the optimized geometries in the triplet and quintet spin states (see Supporting Information). The calculated singlet−triplet energy gaps with the four QM models lie within a few kcal mol^{-1}, while the singlet−quintet energy gaps show somewhat larger fluctuations ranging from 9.1 to 14.3 kcal mol^{-1}. It appears, therefore, that second coordination sphere effects are small and do not lead to significant changes in the geometry and electronic properties of the calculated species.

The optimized geometries in Figure 5 show features typical for a dioxygen bound complex. In all structures the Fe−O distance is 1.880−1.898 Å and hence somewhat shorter than found in a DFT model study (1.906 Å)[16a] and also shorter than typically calculated for iron(II)-superoxo complexes in cytochrome P450 enzymes, where values of 1.940 to 2.002 Å have been reported.[54c,56] On the other hand, the O−O distance calculated for the singlet spin DFT model complex from ref 16a is midway in the range of values from 1.298−1.359 Å shown in Figure 5. The O−O distances for the CDO optimized geometries are close to values reported for heme-based iron(II)-superoxo complexes.[57] Although the three histidine ligands are anchored to the protein backbone, surprisingly the three Fe−N distances are very much alike with a spread of maximally about 0.1 Å. The size of the QM region has very little effect on the optimized geometries of the iron with its direct ligands. Moreover, the QM/MM optimized geometries are very similar to those from a DFT model study[16a] which gave Fe−N_{His86}, Fe−N_{His88}, and Fe−N_{His140} distances of 2.090, 2.055, and 2.014 Å, respectively. The largest difference between the various QM regions and snapshots is found for the dihedral angle between S−Fe−O−O.

In summary, the size of the QM region has very little effect on the optimized geometries of the active-site region and minor effects on the relative energies, and the spin-state ordering is the same in all cases. Nevertheless, to make sure that the choice of the QM region will not affect the conclusions drawn in this paper, we decided to run the complete reaction mechanism calculations with the large QM region R_4.

As further test on basis set effects, we optimized the geometry of ^{1}**A** using QM region R_4 in Sn_{200} and the large TZVP basis set (instead of basis B1). The results displayed in Figure 5 show that identical spin-state energies between the lowest lying singlet, triplet, and quintet spin states are obtained from the QM/MM optimizations with the TZVP and B1 basis sets. Furthermore, the optimized geometries are very similar, without any dramatic differences. Consequently, for the remainder of the calculations, we restricted ourselves to basis set B1 for geometry optimizations. Previous studies on iron(IV)-oxo model complexes and their reactivity patterns reported similar trends in energetics from geometries optimized with a double-ζ quality basis set as compared to a triple-ζ basis set,[58] which further supports our choice of basis set for these types of calculations.

We now address the local environment of the superoxo moiety in ^{1}**A** as calculated with QM(B3LYP/B1)/CHARMM and QM-(B3LYP/TZVP)/CHARMM. Figure 6 shows the relevant parts of the corresponding optimized structures which exhibit similar hydrogen-bonding interactions of the superoxo group with its local environment. The superoxo group is located in a cavity surrounded by the amino acid side chains of Cys_{93}, Leu_{95}, Ile_{133}, His_{155}, Tyr_{157}, and substrate cysteinate. The hydrogen-bonding donor and acceptor groups of the second-sphere amino acids are included in the QM region of the calculations, while Leu_{95} and Ile_{133} are part of the MM region. The distal oxygen atom is involved in hydrogen-bonding interactions with the amine group of substrate cysteinate and with the imidazole group of His_{155} (distances of 2.146−2.257 Å). The sulfur atom of Cys_{93} is located about 3 Å away from the distal oxygen atom O_d, indicating non-negligible electrostatic interactions. Interestingly, the proximal oxygen atom forms a hydrogen bond with the imidazole group of the metal ligand His_{140}. This will force the proximal oxygen atom into a specific orientation, which may be

dx.doi.org/10.1021/ja107514f |*J. Am. Chem. Soc.* 2011, 133, 3869–3882

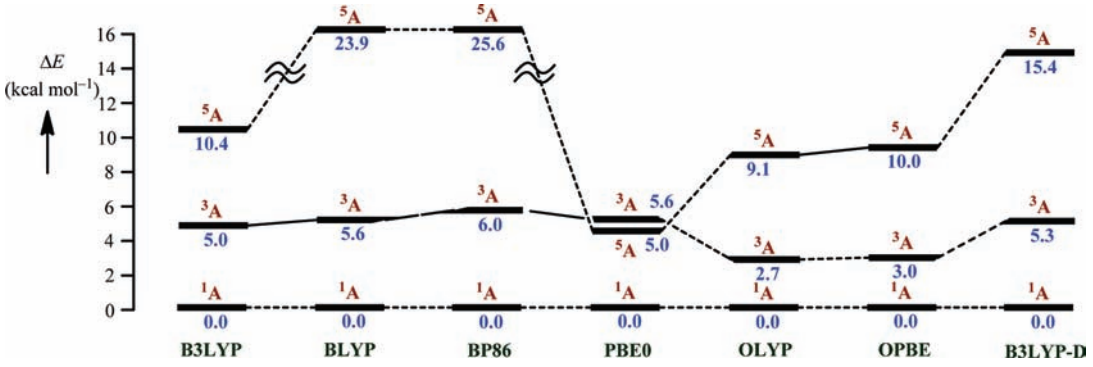

Figure 7. Relative energies (in kcal mol^{-1}) of the lowest-lying singlet, triplet, and quintet spin states of the iron(II)-superoxo complex of CDO (**A**) as calculated with seven different density functional methods. Single-point calculations using basis set B1 on optimized B3LYP/B1 structures were performed using snapshot Sn_{200} and QM region R_4.

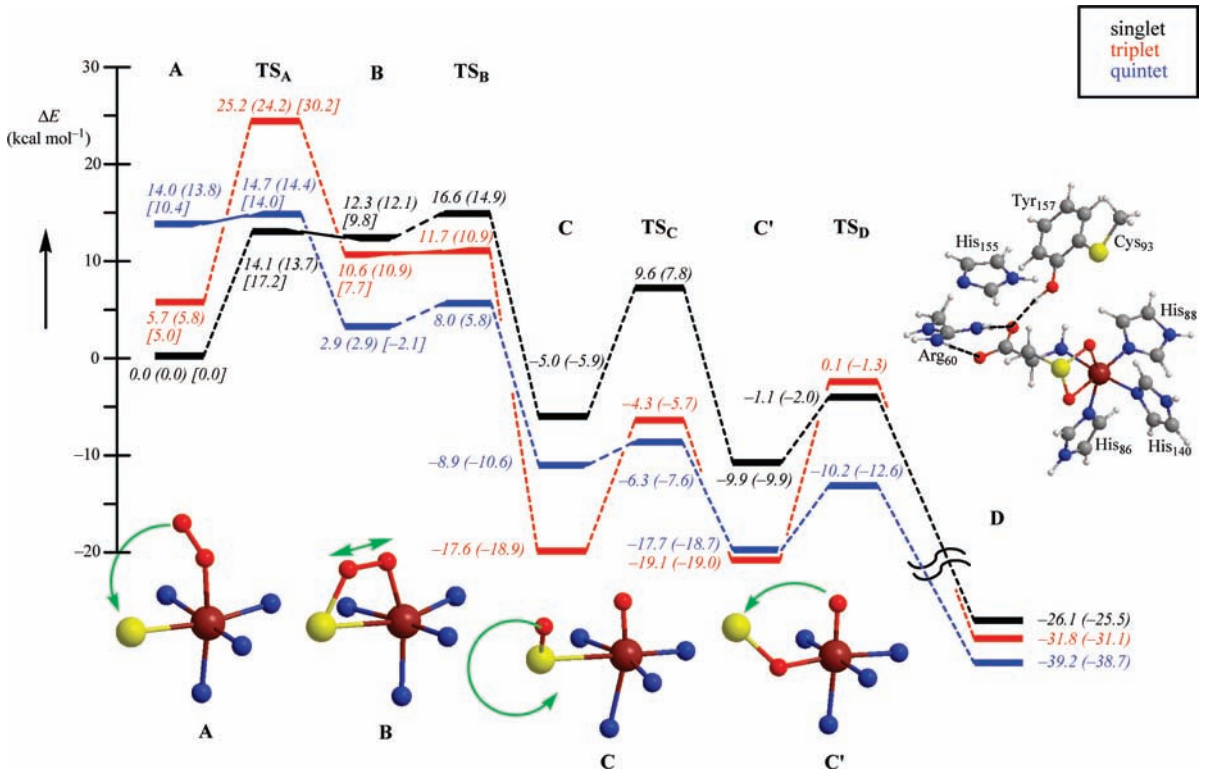

Figure 8. Potential energy profile of dioxygen activation by CDO enzymes starting from the iron(II)-superoxo complex (^{1,3,5}**A**) using QM region R_4. All energies are in kcal mol^{-1} relative to ^{1}**A**. The two values given for each structure represent ΔE and ΔE+ZPE. QM(B3LYP/B2W)/MM energies ΔE were obtained from single-point calculations on QM(B3LYP/B1)/MM optimized geometries, and zero-point energies ZPE were determined at the QM(B3LYP/B1)/MM level; the surface follows the ΔE+ZPE data. Values given in square brackets refer to QM(B3LYP/TZVP)/MM energies ΔE obtained after geometry optimizations at this level.

reason why we were unable to locate the side-on bound isomer of the iron(II)-superoxo or iron(III)-peroxo intermediate. Clearly, the superoxo group in ^{1}**A** is held in position by several moderately strong interactions and is thus expected to be fairly rigid in its local environment.

A final set of calibration calculations were done using seven different density functionals: B3LYP, BLYP, BP86, PBE0, B3LYP-D, OLYP, and OPBE. In transition metal complexes the choice of the density functional can sometimes influence spin-state orderings and relative energies dramatically and should therefore be thoroughly calibrated.[59] Thus, with hybrid functionals such as B3LYP high spin states are generally stabilized, whereas closed-shell configurations tend to be favored with pure density functionals such as BP86. Furthermore, it has been shown that dispersion-corrected density functional methods, such as B3LYP-D, give superior performance in calculating spin-state energetics.[60] To test the sensitivity of our QM/MM results with regard to the chosen functionals, we calculated the lowest-lying singlet, triplet, and quintet spin states of the iron(II)-superoxo bound structure (^{1,3,5}**A**) using seven commonly employed density functionals. Figure 7 displays the spin-state ordering and relative energies obtained on B3LYP/B1 optimized geometries.

All density functionals predict a singlet spin ground state that is separated from the other spin states by at least 2.7 kcal mol^{-1}.

dx.doi.org/10.1021/ja107514f |*J. Am. Chem. Soc.* 2011, 133, 3869–3882

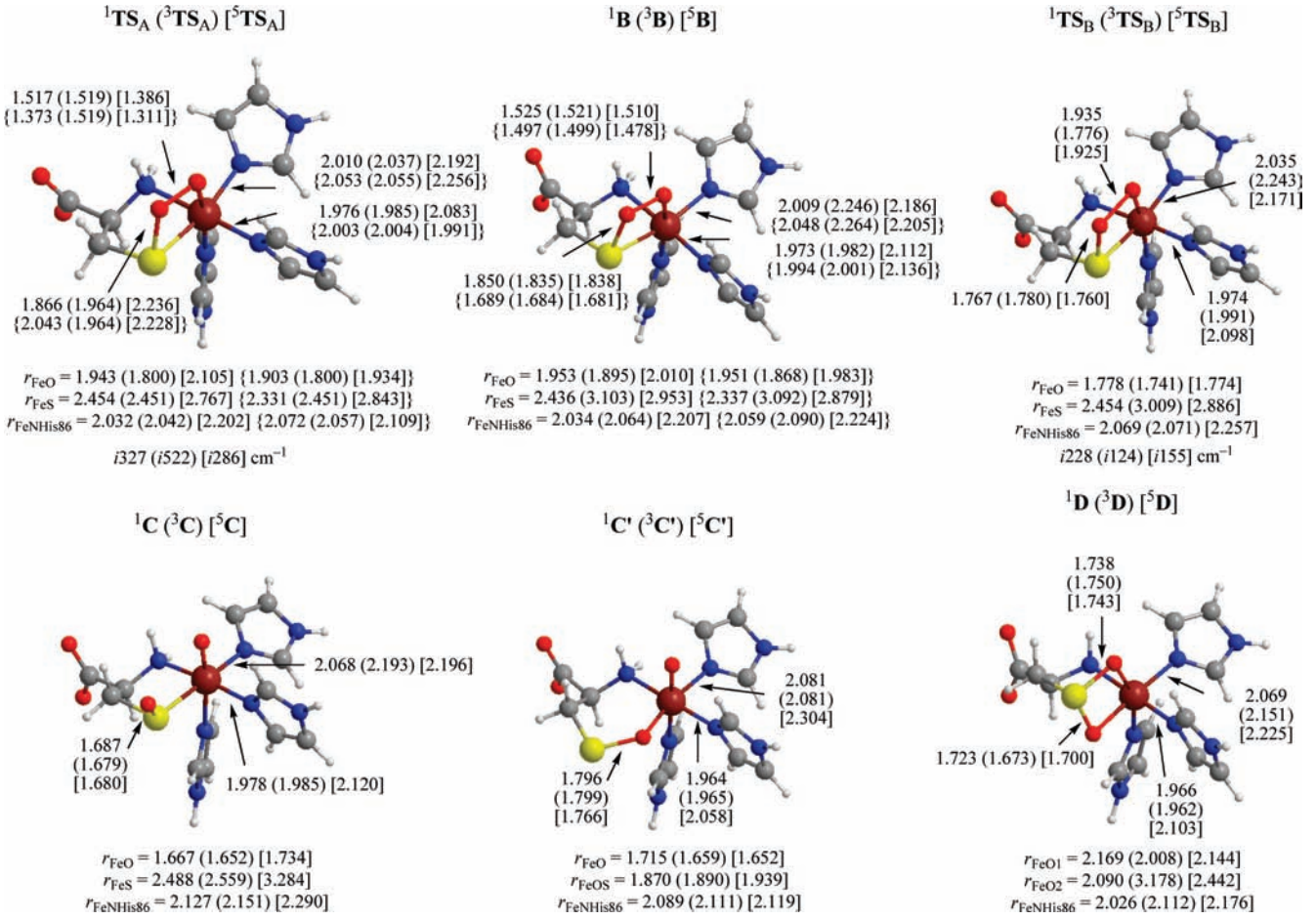

Figure 9. Extracts of the optimized geometries for mechanism I of cysteine dioxygenation by CDO as calculated by QM(B3LYP/B1)/MM using snapshot Sn_{200}. Values are given for the singlet (triplet) [quintet] spin states; the data in curly brackets come from QM(B3LYP/TZVP)/MM geometry optimizations. Bond lengths are given in angstroms and imaginary transition-state frequencies in wavenumbers. All structures depicted here were optimized using QM region R_4. The second-sphere amino acids in the QM region are not shown.

All give the triplet spin state well below the quintet spin state, except for PBE0, where the order is reversed and the energy difference between triplet and quintet is small (only 0.6 kcal mol^{-1}). Consequently, the PBE0 functional is probably least suitable for the studies presented here. On average the triplet state is 4.7 ± 1.3 kcal mol^{-1} above the singlet ground state, with the B3LYP result closest to the average. As expected, there is some fluctuation in the relative energy of the quintet spin state, which is destabilized when using pure density functionals, such as BLYP and BP86. This is a common feature for these types of DFT methods.[59] If we exclude the results obtained with BLYP and BP86, the average singlet−quintet energy gap is 10.0 ± 3.7 kcal mol^{-1}. Again, the B3LYP result seems to be closest to the average. In any event, all methods agree that the quintet spin state is an excited state that lies appreciably above the singlet ground state of the iron(II)-superoxo bound species. In the remainder of this article, we shall use the B3LYP functional exclusively, in view of the present validation and its well-established performance in computational studies of iron containing enzymes.[54c,56]

B. Dioxygen Activation via Mechanism I. Subsequently, we studied the dioxygen activation reaction by cysteinate via Mechanism I (Scheme 2) as calculated with QM/MM methods using snapshot Sn_{200} and the largest QM region R_4 (81 atoms). The calculated potential energy profile is shown in Figure 8, while optimized geometries of the critical points are given in Figure 9. The optimized geometries of the local minima and transition states show little geometric distortion in the second-sphere amino acids included in the QM region. Thus, the hydrogen bond distances between Tyr_{157} and the carboxylic acid group of cysteinate (or its derivative) range between 1.550 and 1.587 Å, and so do salt bridge distances between Arg_{60} and this carboxylate group. The hydrogen bonding between His_{155} and Tyr_{157} is somewhat more flexible, with pertinent distances ranging from 2.518 Å in ^{1}**A** via 2.672 Å in ^{5}**B** to 2.277 Å and 2.048 Å in ^{3}**C** and ^{3}**C**′, respectively. Given this situation, we only show the metal and its ligands in Figure 9, although it should be emphasized that the geometry optimizations were done with QM region R_4, which includes the side chains of Arg_{60}, His_{155}, Tyr_{157}, and Cys_{93}. In all optimized geometries, the proximal oxygen atom forms a hydrogen bond with the imidazole group of His_{140}, which remains twisted during the reaction.

As follows from Figure 8, the reaction takes place via multistate reactivity patterns on competing singlet, triplet, and quintet spin-state surfaces, similar to substrate hydroxylation by heme and nonheme iron(IV)-oxo oxidants.[61] Although the singlet spin state is the ground state for the iron(II)-superoxo complex (**A**), a spin-state crossing to the quintet spin state initiates the reaction

dx.doi.org/10.1021/ja107514f |J. Am. Chem. Soc. 2011, 133, 3869–3882

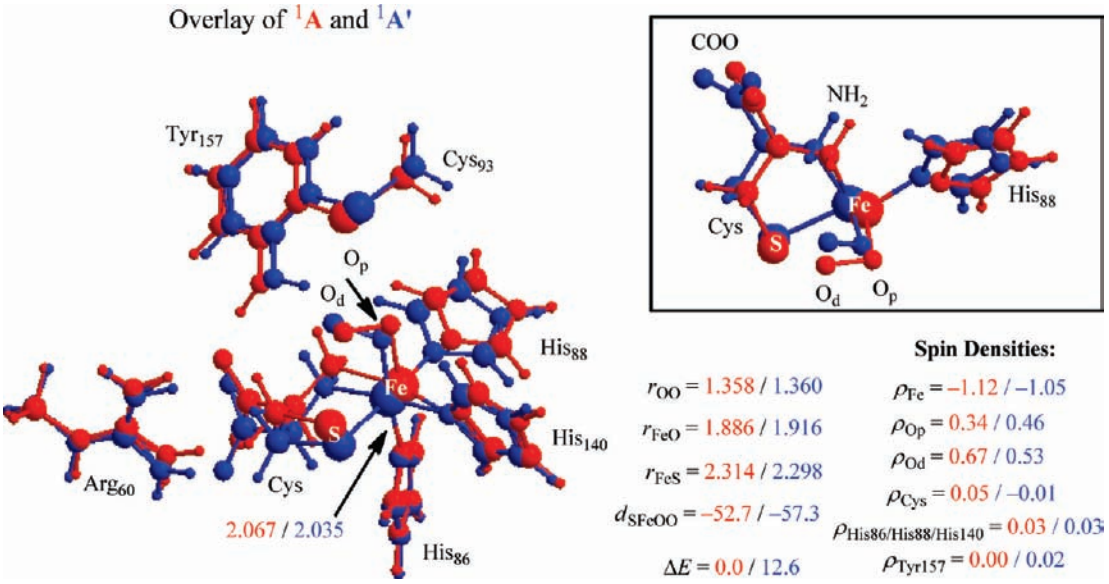

Figure 10. Overlay of the optimized geometries of ^{1}**A** (in red) and ^{1}**A**′ (in blue) obtained with QM region R_4. The inset shows the FeO_2 with cysteinate and opposing histidine ligands in a different view. Selected bond distances are in angstroms and dihedral angles in degrees. Also shown is the relative energy between ^{1}**A** and ^{1}**A**′ and the group spin densities calculated at the QM(B3LYP/B1)/MM level.

to form a quintet spin ring structure (^{5}**B**). This crossing occurs slightly before (after) the transition state ^{1}**TS**$_A$ for S−O bond formation when using the TZVP (B1) basis set for geometry optimization. The resulting quintet intermediate with a four-membered ring (^{5}**B**) undergoes dioxygen bond cleavage leading to a sulfoxide and an iron-oxo species (**C**) via a barrier of ΔE+ZPE = 2.9 kcal mol^{-1} (B3LYP/B2W). This reaction is highly exothermic at B3LYP/B2W level, and 13.5 kcal mol^{-1} of energy is released in the quintet spin state. Intermediate **C** has a lower-lying triplet state, that is, ^{3}**C** is below ^{5}**C** by 8.3 kcal mol^{-1} (B3LYP/B2W). The sulfoxide intermediate ^{5}**C** probably has a short lifetime since only a small reaction barrier ^{5}**TS**$_C$ of 3.0 kcal mol^{-1} separates it from the rotated sulfoxide structure ^{5}**C**′. During the rotation from **C** to **C**′ the Fe−S bond in **C** breaks, and a rotation around the C−C bond moves the sulfur atom away from the metal and gives the oxygen atom the opportunity to bind instead. In the resulting structure (**C**′) the sulfur atom is freely accessible for the second oxygen atom, while the sulfoxide oxygen atom binds to iron. On the triplet spin-state surface this barrier is substantially higher (13.2 kcal mol^{-1} via ^{3}**TS**$_C$). The rotated sulfoxide structure **C**′ also has a triplet spin ground state with the quintet spin state 0.3 kcal mol^{-1} higher in energy. Both **C** and **C**′ are thus iron(IV)-oxo complexes with a triplet spin ground state. This spin-state ordering is supported by experimental and computational studies of nonheme iron(IV)-oxo complexes that tend to give a triplet spin ground state.[62,63] By contrast, the iron(IV)-oxo species of TauD has a quintet spin ground state due to a 2His/1Asp ligand system that decreases the $\pi^*_{xy}/\sigma^*_{x^2-y^2}$ energy gap through strong ligand interactions and hence stabilizes the quintet state over the triplet.[63] The $\sigma^*_{x^2-y^2}$ orbital is lowered in energy when strong anionic ligands are bound to the metal in the *xy* plane of symmetry (perpendicular to the Fe(IV)═O axis). In structures **C** and **C**′ in CDO, the *xy* plane of symmetry contains two histidine ligands and a sulfoxide group, which are all neutral. By contrast, in TauD there are two carboxylic acid groups bound to the metal in the *xy* plane, and as a consequence, the $\sigma^*_{x^2-y^2}$ orbital is lowered in energy and a quintet ground state is created, while structures **C** and **C**′ in CDO have a triplet ground state. The final step leading to cysteine sulfinic acid products (**C**′ → **D**) has the smallest barrier on the quintet spin-state surface (6.1 kcal mol^{-1} at B3LYP/B2W). Previous DFT studies of the reactivity of nonheme iron(IV)-oxo complexes also gave lower reaction barriers in the quintet spin state as compared to the triplet spin state, in agreement with what is found here.[24,61b,63,64] The product complex has a quintet ground state. The overall reaction exothermicity is 38.7 kcal mol^{-1} with B3LYP/B2W. This value compares well with reaction exothermicities calculated for substrate hydroxylation and epoxidation by iron(IV)-oxo oxidants, where the reaction exothermicities were shown to be governed by the energies of the bonds that are broken and formed.[34c,34d,58c]

The overall reaction mechanism calculated with QM-(B3LYP)/MM is similar to that reported before using DFT model complexes,[16] although there are some significant differences. However, these differences do not affect the product distributions or the rate-determining steps in the mechanism. All our theoretical studies predict a singlet spin iron(II)-superoxo complex that undergoes S−O bond formation with cysteinate via a spin crossing to the quintet spin-state surface. The rate-determining barrier in all cases is this spin state crossing to ^{5}**TS**$_A$ on the path to the ring structure. In the following steps, we find multistate reactivity patterns on competing triplet and quintet spin-state surfaces with QM/MM, whereas the DFT model calculations[16] predict the quintet and triplet spin states of **C**, **C**′, and **D** to be well separated with a quintet spin ground state. On the quintet spin-state surface, each intermediate is computed to be lower in energy than its precursor, at both levels.

We note that full QM/MM geometry optimizations with UB3LYP/TZVP closely reproduce the results obtained with UB3LYP/B1 and confirm the corresponding mechanistic conclusions. Test calculations with QM regions R_1 and R_4 further

dx.doi.org/10.1021/ja107514f |*J. Am. Chem. Soc.* 2011, 133, 3869–3882

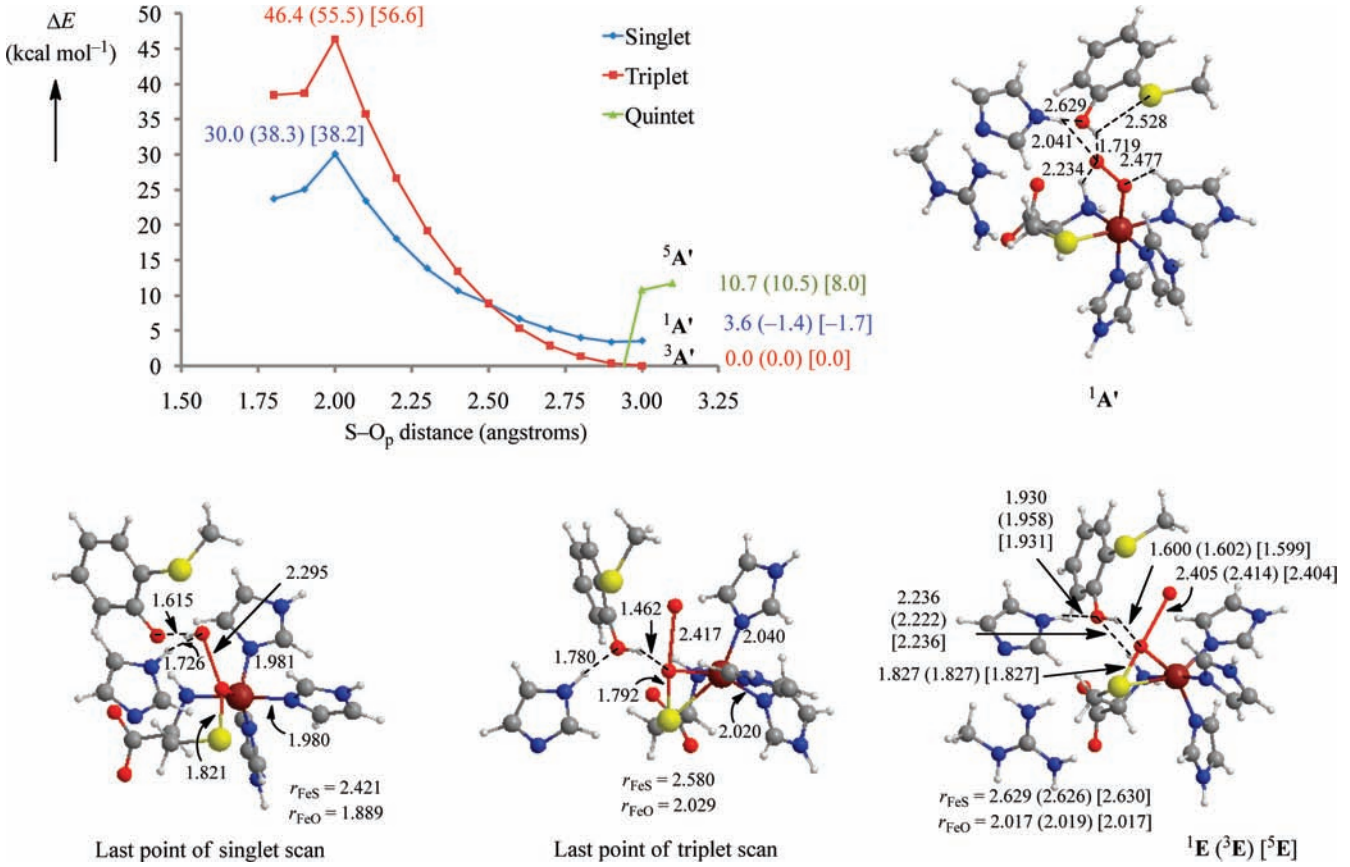

Figure 11. Geometry scans for attack of sulfur on the proximal oxygen atom. Single-point QM(B3LYP)/MM energies obtained with the B1 (B2W) [TZVP] basis set on QM(B3LYP/B1)/MM-optimized geometries using QM region R_4, given in kcal mol^{-1} relative to ^{3}**A**′. Also shown are the optimized geometries of ^{1}**A**′, of the last point of the singlet and triplet geometry scans, and of the "persulfenate"' structures ^{1,3,5}**E,** with bond lengths given in angstroms.

indicate that the results are not too sensitive with regard to the choice of the QM region (see Supporting Information for further details).

C. Dioxygen Activation via Mechanism II. Crystal structure analysis led to the proposal of an alternative mechanism for cysteine activation by CDO enzymes (mechanism II in Scheme 2), where the sulfur group of cysteinate attacks the proximal oxygen atom to form a persulfenate complex, facilitated through a hydrogen bonding interaction of the distal oxygen atom with the phenol proton of Tyr_{157}.[25] To test this hypothesis, we first optimized the geometries (using QM region R_4) of the rotated dioxygen bound complexes ^{1,3,5}**A**′, which contain a direct hydrogen bond between the phenol OH group of Tyr_{157} and the distal oxygen atom of O_2. These structures are significantly higher in energy than structure ^{1}**A**, by 12.5, 9.0, and 19.7 kcal mol^{-1} at the QM(B3LYP/B1)/MM level of theory. Figure 10 displays the overlay of optimized geometry of ^{1}**A**′ and ^{1}**A** as calculated with QM/MM using B3LYP/B1.

Obviously, ^{1}**A** and ^{1}**A**′ are very much alike in their geometric features. The Fe−S distance is somewhat shortened by 0.016 Å, while the Fe−O distance is slightly elongated by 0.030 Å when going from ^{1}**A** to ^{1}**A**′. The key difference, however, is the rotation of the phenol OH group of Tyr_{157}, with a switch of the hydrogen bond from the carboxylic acid group of the substrate in ^{1}**A** to the distal oxygen atom of the superoxo group in ^{1}**A**′. The corresponding QM(B3LYP/B1)/MM hydrogen bond distances are 1.585 Å in ^{1}**A** and 1.719 Å in ^{1}**A**′. The latter hydrogen bond is obviously weaker, and hence ^{1}**A**′ is less stable than ^{1}**A**. Because of the reorientation of the Tyr residue, the dioxygen moiety is bent toward the Tyr group and the dihedral angle S−Fe−O_p−O_d increases to −57.3°.

Electronically, the two isomers ^{1}**A** and ^{1}**A**′ are virtually identical with one unpaired electron each on a metal based orbital (π^*_{xz}) and an antibonding orbital along the O−O bond (π^*_{OO}), whereby the former orbital contains a β-spin electron and the latter an α-spin electron. Reorientation of the phenol OH group of Tyr_{157} results in sizable loss of polarization on the individual oxygen atoms in the dioxygen group, and the spin densities change from ρ_{Op} = 0.34 and ρ_{Od} = 0.67 in ^{1}**A** to ρ_{Op} = 0.46 and ρ_{Od} = 0.53 in ^{1}**A**′. At the same time, the iron loses some of its unpaired spin density (0.07 units) and so does the cysteinate substrate (0.06 units). This change in polarization may affect the reaction mechanism of cysteine activation.

Subsequently, we investigated the attack of the proximal oxygen atom (O_p) on the sulfur atom of substrate cysteinate. The computed geometry scans and the optimized geometries of the critical points are shown in Figure 11. They indicate high-energy mechanisms with reaction barriers well over 30 kcal mol^{-1} on the singlet and triplet spin-state surfaces. These barriers are much higher than those obtained for mechanism I (see Figure 8) which is thus clearly favored. In the case of the quintet spin state, the geometry scan failed and led to the formation of a ring structure similar to structure ^{5}**B** discussed in the previous section. The initial points of the scan on the quintet surface are, however, already higher in energy than the rate-limiting barriers of

dx.doi.org/10.1021/ja107514f |*J. Am. Chem. Soc.* 2011, 133, 3869–3882

Scheme 3. Proposed Mechanism of Cysteine Dioxygenation by CDO Enzymes As Elucidated by QM/MM Studies

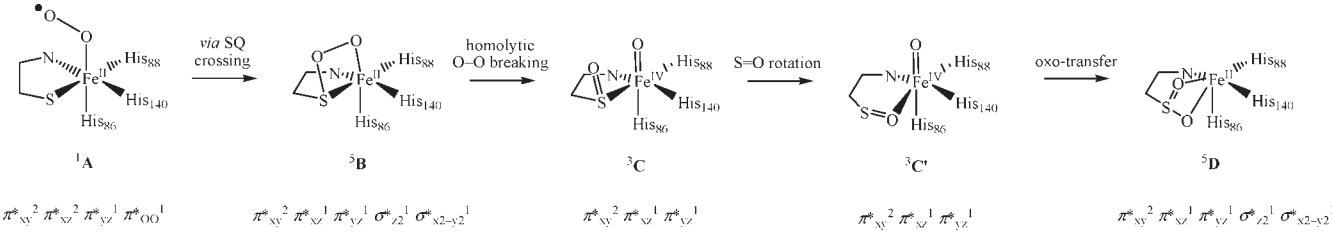

mechanism I. In conclusion, our QM/MM calculations thus rule out the persulfenate structure as an intermediate in the catalytic cycle of CDO enzymes.

Optimized geometries starting from the last points of these geometry scans are included at the bottom of Figure 11. These QM(B3LYP/B1)/MM geometry optimizations were done without geometric constraints. In both the singlet and the triplet, the dioxygen bond weakens dramatically to well over 2 Å. In the triplet spin state the dioxygen bond lengthens to 2.417 Å, so that this species is actually a sulfoxide with a nearby oxygen atom rather than the expected persulfenate structure. The proximal oxygen atom O_p is still held in position by a donating hydrogen bond from the phenol group of Tyr_{157}. The Fe−S distance of 2.580 Å and the S−O distance of 1.792 Å (Figure 11) indicate structural similarities with ^{3}**C** (Figure 9). In the singlet spin state, these distances are similar (r_{FeS} = 2.421 Å and r_{SO} = 1.821 Å), but the dioxygen distance is shorter (2.295 Å). In addition, the distal oxygen atom has abstracted a proton from Tyr_{157} to give an OH^- anion nearby a sulfoxide group. At the same time, the donating hydrogen bond from His_{155} is shifted from the phenolate oxygen atom in the triplet spin-state product to the OH^- group in the singlet spin state. It appears, therefore, that the singlet persulfenate structure is not a stable moiety and will abstract a proton readily from a nearby proton source.

To ascertain that there is no alternative persulfenate structure with an intact dioxygen bond, we manually created suitable starting geometries of a persulfenate bound complex, ^{1,3,5}**E**, which however collapsed upon unconstrained full optimization to structures similar to those found after a full geometry optimization of the last point of the geometry scans (see data given at the bottom right of Figure 11). The persulfenate-type structures ^{1,3,5}**E** thus rearrange in a barrierless process to sulfoxides with a nearby oxygen atom. Hence, according to the QM/MM calculations, persulfenate species are not stable in the CDO enzyme active-site environment, and the proposed mechanism II is therefore not supported. It seems likely the experimentally found "persulfenate" structure actually refers to a protonated species.

D. Electronic Characterization of Mechanism I. To summarize the QM/MM reaction mechanism of cysteine dioxygenation by CDO enzymes, we now address the changes in electronic structure during the reaction. The mechanism that emerges from the QM/MM calculations is given in Scheme 3, which specifies under each species the orbital occupation of the dominant electronic configuration. The reaction starts with a spin-state crossing from the singlet spin state to the quintet spin state with an electron transfer from π^*_{xz} to $\sigma^*_{z^2}$. This happens during attack of the distal oxygen atom on the sulfur atom of the substrate to form a dioxygen bridged structure **B**. On the quintet spin state this ring closure involves a homolytic S−O bond formation where the radical on the distal oxygen atom pairs up with one of the electrons from a lone-pair on sulfur, while the other electron from the lone-pair is transferred to the $\sigma^*_{x^2-y^2}$ orbital, hence ^{5}**B** has orbital occupation $\pi^*_{xy}{}^2\ \pi^*_{xz}{}^1\ \pi^*_{yz}{}^1\ \sigma^*_{z^2}{}^1\ \sigma^*_{x^2-y^2}{}^1$. Indeed, the conversion of ^{1}**A** to ^{5}**B** leads to an elongation of the Fe−S bond from 2.314 to 2.953 Å indicative of occupation of the $\sigma^*_{z^2}$ orbital with an extra electron (from ^{1}**A** to ^{5}**A**) and transfer of an electron from π^*_{OO} to $\sigma^*_{x^2-y^2}$ (from ^{5}**A** to ^{5}**B**). Accordingly, the radical character on the sulfur atom is reduced and the spin density of the cysteinate group changes from ρ_{Cys} = −0.44 in ^{5}**A** to ρ_{Cys} = −0.30 in ^{5}**TS**$_A$ to ρ_{Cys} = 0.09 in ^{5}**B** (B3LYP/B2W), whereas the spin density on the dioxygen group drops from ρ_{OO} = 0.51 in ^{5}**A** to ρ_{OO} = 0.11 in ^{5}**B**.

Dioxygen bond breaking in ^{5}**B** gives an iron(IV)-oxo complex with sulfoxide in the triplet spin state (^{3}**C**) with electronic configuration $\pi^*_{xy}{}^2\ \pi^*_{xz}{}^1\ \pi^*_{yz}{}^1$. By contrast, on the quintet spin-state surface ^{5}**C** is an iron(III)-oxo complex with a sulfoxide radical with orbital occupation $\pi^*_{xy}{}^1\ \pi^*_{xz}{}^1\ \pi^*_{yz}{}^1\ \sigma^*_{z^2}{}^1\ \sigma^*_{x^2-y^2}{}^1\ \pi^*_{SO}{}^1$. In the triplet manifold, ^{3}**C** carries considerable spin density on the sulfoxide moiety, ρ_{SO} = −0.51 (B3LYP/B2W). Rotation of the sulfoxide group gives pure iron(IV)-oxo sulfoxide complexes ^{3}**C**′ and ^{5}**C**′ with electronic configuration $\pi^*_{xy}{}^2\ \pi^*_{xz}{}^1\ \pi^*_{yz}{}^1$ and $\pi^*_{xy}{}^1\ \pi^*_{xz}{}^1\ \pi^*_{yz}{}^1\ \sigma^*_{x^2-y^2}{}^1$, respectively. In the final step of the mechanism, the oxygen atom is transferred to the sulfoxide, and two electrons are relayed from the sulfoxide to the metal, which is reduced to the iron(II) oxidation state with orbital occupation $\pi^*_{xy}{}^2\ \pi^*_{xz}{}^2\ \pi^*_{yz}{}^1\ \sigma^*_{z^2}{}^1$ and $\pi^*_{xy}{}^2\ \pi^*_{xz}{}^1\ \pi^*_{yz}{}^1\ \sigma^*_{z^2}{}^1\ \sigma^*_{x^2-y^2}{}^1$, respectively, for ^{3}**D** and ^{5}**D**.

In summary, the QM/MM calculations thus predict multistate reactivity patterns, with close-lying singlet, triplet, and quintet spin states participating in the reaction mechanism. The exact nature of the reaction mechanism will depend on the efficiency of spin-state crossings between these spin-state surfaces. If these crossings are facile such that the system can always access the lowest energy surface, the reaction will proceed along the sequence ^{1}**A**, ^{5}**TS**$_A$, ^{5}**B**, ^{5}**TS**$_B$, ^{3}**C**, ^{5}**TS**$_C$, ^{3}**C**′, and ^{5}**TS**$_D$ to give ^{5}**D**. In this mechanism the rate-determining step is the spin crossing from singlet to quintet around **TS**$_A$. If we assume that the initial singlet−quintet spin crossing is spin-forbidden such that the quintet state is not accessible, we arrive at an alternative mechanism where the ferric-dioxygen complex (^{1}**A**) reacts on the singlet spin-state surface to form ^{1}**B**, followed by a surface crossing to ^{3}**B**. The reaction then continues on the triplet spin-state surface via ^{3}**TS**$_B$, ^{3}**C**, ^{3}**TS**$_C$ and ^{3}**C**′ before a spin-state crossing to the quintet spin state gives ^{5}**D** products. In this alternative mechanism, the first step is again rate-determining (^{1}**TS**$_A$, 14.1 kcal mol^{-1}), although the subsequent transition state ^{3}**TS**$_C$ is only 0.8 kcal mol^{-1} lower in energy (B3LYP/B2W). In

dx.doi.org/10.1021/ja107514f |J. Am. Chem. Soc. 2011, 133, 3869–3882

both cases, mechanism I involves a rate-determining spin-state crossing during the conversion from **A** to **B**.

IV. CONCLUSIONS

Quantum mechanics/molecular mechanics calculations on cysteine activation by CDO enzymes are reported. We have considered two mechanisms starting from the dioxygen bound intermediate, namely, attack of the proximal or distal oxygen atoms of O_2 on the sulfur of cysteinate. In agreement with earlier DFT modeling of active-site structures, the QM/MM calculations favor mechanism I with an initial singlet−quintet crossing and subsequent transformations on the quintet surface that involve the transfer of the distal oxygen atom to yield a sulfoxide bound to an iron(IV)-oxo species followed by the formation of cysteine sulfinic acid bound to an iron(III) group. Calculations on mechanism II have identified only high-energy pathways that will not be able to compete with mechanism I.

■ ASSOCIATED CONTENT

Supporting Information. Ninety-four tables with group spin densities, charges, and relative energies of all complexes described in this work; eight figures with geometry scans and MD simulations; refs 32, 47, and 52 in full. This material is available free of charge via the Internet at http://pubs.acs.org.

■ AUTHOR INFORMATION

Corresponding Author
dkclcre@yahoo.com; sam.devisser@manchester.ac.uk

■ ACKNOWLEDGMENT

D.K. holds a Ramanujan Fellowship from the Department of Science and Technology (DST), New Delhi (India), and acknowledges its financial support (Research Grants SR/S2/RJN-11/2008 and SR/S1/PC-58/2009).

■ REFERENCES

(1) (a) Solomon, E. I.; Brunold, T. C.; Davis, M. I.; Kemsley, J. N.; Lee, S.-K.; Lehnert, N.; Neese, F.; Skulan, A. J.; Yang, Y.-S.; Zhou, J. *Chem. Rev.* **2000**, *100*, 235–349. (b) Bugg, T. D. H. *Curr. Opin. Chem. Biol.* **2001**, *5*, 550–555. (c) Costas, M.; Mehn, M. P.; Jensen, M. P.; Que, L., Jr. *Chem. Rev.* **2004**, *104*, 939–986. (d) Bruijnincx, P. C. A.; van Koten, G.; Klein Gebbink, R. J. M. *Chem. Soc. Rev.* **2008**, *37*, 2716–2744. (e) Bugg, T. D. H.; Ramaswamy, S. *Curr. Opin. Chem. Biol.* **2008**, *12*, 134–140.

(2) (a) Krebs, C.; Fujimori, D. G.; Walsh, C. T.; Bollinger, J. M., Jr. *Acc. Chem. Res.* **2007**, *40*, 484–492. (b) Schofield, C. J.; Zhang, Z. *Curr. Opin. Chem. Biol.* **1999**, *9*, 722–731. (c) Bugg, T. D. H. *Tetrahedron* **2003**, *59*, 7075–7101.

(3) (a) Trewick, S. C.; Henshaw, T. F.; Hausinger, R. P.; Lindahl, T.; Sedgwick, B. *Nature* **2002**, *419*, 174–178. (b) Falnes, P. Ø.; Johansen, R. F.; Seeberg, E. *Nature* **2002**, *419*, 178–182. (c) Duncan, T.; Trewick, S. C.; Koivisto, P.; Bates, P. A.; Lindahl, T.; Sedgwick, B. *Proc. Natl. Acad. Sci. U.S.A.* **2002**, *99*, 16660–16665. (d) Aas, P. A.; Otterlei, M.; Falnes, P. Ø.; Vågbø, C. B.; Skorpen, F.; Akbari, M.; Sundheim, O.; Bjørås, M.; Slupphaug, G.; Seeberg, E.; Krokan, H. E. *Nature* **2003**, *421*, 859–863. (e) Mishina, Y.; Duguid, E. M.; He, C. *Chem. Rev.* **2006**, *106*, 215–232.

(4) Chowdhury, R.; Hardy, A.; Schofield, C. J. *Chem. Soc. Rev.* **2008**, *37*, 1308–1319.

(5) Que, L., Jr. *Nat. Struct. Biol.* **2000**, *7*, 182–184.

(6) (a) Ryle, M. J.; Hausinger, R. P. *Curr. Opin. Chem. Biol.* **2002**, *6*, 193–201. (b) O'Brien, J. R.; Schuller, D. J.; Yang, V. S.; Dillard, B. D.; Lanzilotta, W. N. *Biochemistry* **2003**, *42*, 5547–5554. (c) Bollinger, J. M., Jr.; Price, J. C.; Hoffart, L. M.; Barr, E. W.; Krebs, C. *Eur. J. Inorg. Chem.* **2005**, 4245–4254. (d) Abu-Omar, M. M.; Loaiza, A.; Hontzeas, N. *Chem. Rev.* **2005**, *105*, 2227–2252.

(7) (a) Sono, M.; Roach, M. P.; Coulter, E. D.; Dawson, J. H. *Chem. Rev.* **1996**, *96*, 2841–2888.(b) *The Porphyrin Handbook*; Kadish, K. M., Smith, K. M., Guilard, R., Eds.; Academic Press: San Diego, CA, 2000. (c) Groves, J. T. *Proc. Natl. Acad. Sci. U.S.A.* **2003**, *100*, 3569–3574. (d) Guengerich, F. P. *Chem. Res. Toxicol.* **2001**, *14*, 611–650.(e) *Cytochrome P450: Structure, Mechanism and Biochemistry*, 3rd ed.; Ortiz de Montellano, P. R., Ed.; Kluwer Academic/Plenum Publishers: New York, 2004. (f) Munro, A. W.; Girvan, H. M.; McLean, K. J. *Nat. Prod. Rep.* **2007**, *24*, 585–609. (g) Nam, W. *Acc. Chem. Res.* **2007**, *40*, 522–531.

(8) (a) Proshlyakov, D. A.; Henshaw, T. F.; Monterosso, G. R.; Ryle, M. J.; Hausinger, R. P. *J. Am. Chem. Soc.* **2004**, *126*, 1022–1023. (b) Riggs−Gelasco, P. J.; Price, J. C.; Guyer, R. B.; Brehm, J. H.; Barr, E. W.; Bollinger, J. M., Jr.; Krebs, C. *J. Am. Chem. Soc.* **2004**, *126*, 8108–8109. (c) Hoffart, L. M.; Barr, E. W.; Guyer, R. B.; Bollinger, J. M., Jr.; Krebs, C. *Proc. Natl. Acad. Sci. U.S.A.* **2006**, *103*, 14738–14743.

(9) Straganz, G. D.; Nidetzky, B. *ChemBioChem.* **2006**, *7*, 1536–1548.

(10) Straganz, G. D.; Nidetzky, B. *J. Am. Chem. Soc.* **2005**, *127*, 12306–12314.

(11) Gopal, B.; Madan, L. L.; Betz, S. F.; Kossiakoff, A. A. *Biochemistry* **2005**, *44*, 193–201.

(12) (a) Stipanuk, M. H. *Annu. Rev. Nutr.* **2004**, *24*, 539–577. (b) Joseph, C. A.; Maroney, M. J. *Chem. Commun.* **2007**, 3338–3349.

(13) Perry, T. L.; Norman, M. G.; Yong, V. W.; Whiting, S.; Crichton, J. U.; Hansen, S.; Kish, S. *J. Ann. Neurol.* **1985**, *18*, 482–489.

(14) Heafield, M. T.; Fearn, S.; Steventon, G. B.; Waring, R. H.; Williams, A. C.; Sturman, S. G. *Neurosci. Lett.* **1990**, *110*, 216–220.

(15) (a) McCoy, J. G.; Bailey, L. J.; Bitto, E.; Bingman, C. A.; Aceti, D. J.; Fox, B. G.; Phillips, G. N., Jr. *Proc. Natl. Acad. Sci. U.S.A.* **2006**, *103*, 3084–3089. (b) Simmons, C. R.; Liu, Q.; Huang, Q.; Hao, Q.; Begley, T. P.; Karplus, P. A.; Stipanuk, M. H. *J. Biol. Chem.* **2006**, *281*, 18723–18733. (c) Pierce, B. D.; Gardner, J. D.; Bailey, L. J.; Brunold, T. C.; Fox, B. G. *Biochemistry* **2007**, *46*, 8569–8578. (d) Gardner, J. D.; Pierce, B. S.; Fox, B. G.; Brunold, T. C. *Biochemistry* **2010**, *49*, 6033–6041.

(16) (a) Aluri, S.; de Visser, S. P. *J. Am. Chem. Soc.* **2007**, *129*, 14846–14847. (b) de Visser, S. P.; Straganz, G. D. *J. Phys. Chem. A* **2009**, *113*, 1835–1846.

(17) (a) Werner, M.; Birner, G.; Dekant, W. *Chem. Res. Toxicol.* **1996**, *9*, 41–49. (b) Madan, A.; Parkinson, A.; Faiman, M. D. *Drug Metab. Dispos.* **1995**, *23*, 1153–1158. (c) Goto, Y.; Matsui, T.; Ozaki, S.-i.; Watanabe, Y.; Fukuzumi, S. *J. Am. Chem. Soc.* **1999**, *121*, 9497–9502. (d) Kato, S.; Yang, H.-J.; Ueno, T.; Ozaki, S.-i.; Phillips, G. N., Jr.; Fukuzumi, S.; Watanabe, Y. *J. Am. Chem. Soc.* **2002**, *124*, 8506–8507. (e) Usmani, K. A.; Karoly, E. D.; Hodgson, E.; Rose, R. L. *Drug Metab. Dispos.* **2004**, *32*, 333–339. (f) Furnes, B.; Schlenk, D. *Drug Metab. Dispos.* **2005**, *33*, 214–218.

(18) Kovacs, J. A. *Chem. Rev.* **2004**, *104*, 825–848.

(19) Heinrich, L.; Mary-Verla, A.; Li, Y.; Vaissermann, J.; Chottard, J.-C. *Eur. J. Inorg. Chem.* **2001**, 2203–2206.

(20) For examples on biomimetic nitrile hydratases, see: (a) Farmer, P. J.; Solouki, T.; Mills, D. K.; Soma, T.; Russell, D. H.; Reibenspies, J. H.; Darensbourg, M. Y. *J. Am. Chem. Soc.* **1992**, *114*, 4601–4605. (b) Farmer, P. J.; Verpeaux, J.-N.; Amatore, C.; Darensbourg, M. Y.; Musie, G. *J. Am. Chem. Soc.* **1994**, *116*, 9355–9356. (c) Grapperhaus, C. A.; Darensbourg, M. Y. *Acc. Chem. Res.* **1998**, *31*, 451–459. (d) Harrop, T. C.; Mascharak, P. K. *Acc. Chem. Res.* **2004**, *37*, 253–260. (e) Chohan, B. S.; Shoner, S. C.; Kovacs, J. A.; Maroney, M. J. *Inorg. Chem.* **2004**, *43*, 7726–7734. (f) Li, B.; Liu, T.; Singleton, M. L.; Darensbourg, M. Y. *Inorg. Chem.* **2009**, *48*, 8393–8403. (g) Rose, M. J.; Betterley, N. M.; Mascharak, P. K. *J. Am. Chem. Soc.* **2009**, *131*, 8340–8341. (h) McDonald, A. R.; Bukowski, M. R.; Farquhar, E. R.; Jackson, T. A.; Koehntop, K. D.; Seo, M. S.; De Hont, R. F.; Stubna, A.; Halfen, J. A.;

Münck, E.; Nam, W.; Que, L., Jr. *J. Am. Chem. Soc.* **2010**, *132*, 17118–17129.
(21) Jiang, Y.; Widger, L. R.; Kasper, G. D.; Siegler, M. A.; Goldberg, D. P. *J. Am. Chem. Soc.* **2010**, *132*, 12214–12215.
(22) Ye, S.; Wu, X.; Wei, L.; Tang, D.; Sun, P.; Bartlam, M.; Rao, Z. *J. Biol. Chem.* **2007**, *282*, 3391–3402.
(23) Dominy, J. E., Jr.; Hwang, J.; Guo, S.; Hirschberger, L. L.; Zhang, S.; Stipanuk, M. H. *J. Biol. Chem.* **2008**, *283*, 12188–12201.
(24) (a) de Visser, S. P. *Angew. Chem., Int. Ed.* **2006**, *45*, 1790–1793. (b) de Visser, S. P. *J. Am. Chem. Soc.* **2006**, *128*, 9813–9824. (c) de Visser, S. P. *Chem. Commun.* **2007**, 171–173. (d) de Visser, S. P. *Coord. Chem. Rev.* **2009**, *253*, 754–768.
(25) Simmons, C. R.; Krishnamoorthy, K.; Granett, S. L.; Schuller, D. J.; Dominy, J. E., Jr.; Begley, T. P.; Stipanuk, M. H.; Karplus, P. A. *Biochemistry* **2008**, *47*, 11390–11392.
(26) For a recent review on QM/MM methods, see: Senn, H. M.; Thiel, W. *Angew. Chem., Int. Ed.* **2009**, *48*, 1198–1229.
(27) (a) Schöneboom, J. C.; Lin, H.; Reuter, N.; Thiel, W.; Cohen, S.; Ogliaro, F.; Shaik, S. *J. Am. Chem. Soc.* **2002**, *124*, 8142–8151. (b) Schöneboom, J. C.; Cohen, S.; Lin, H.; Shaik, S.; Thiel, W. *J. Am. Chem. Soc.* **2004**, *126*, 4017–4034. (c) Bathelt, C. M.; Zurek, J.; Mulholland, A. J.; Harvey, J. N. *J. Am. Chem. Soc.* **2005**, *127*, 12900–12908.
(28) Lundberg, M.; Morokuma, K. *J. Phys. Chem. B* **2007**, *111*, 9380–9389.
(29) (a) Cohen, S.; Kumar, D.; Shaik, S. *J. Am. Chem. Soc.* **2006**, *128*, 2649–2653. (b) Altarsha, M.; Benighaus, T.; Kumar, D.; Thiel, W. *J. Am. Chem. Soc.* **2009**, *131*, 4755–4763. (c) Altarsha, M.; Benighaus, T.; Kumar, D.; Thiel, W. *J. Biol. Inorg. Chem.* **2010**, *15*, 361–372.
(30) Godfrey, E.; Porro, C. S.; de Visser, S. P. *J. Phys. Chem. A* **2008**, *112*, 2464–2468.
(31) (a) Schöneboom, J. C.; Thiel, W. *J. Phys. Chem. B* **2004**, *108*, 7468–7478. (b) Altun, A.; Thiel, W. *J. Phys. Chem. B* **2005**, *109*, 1268–1280.
(32) MacKerell, A. D.; et al. *J. Phys. Chem. B* **1998**, *102*, 3586–3616 (see the Supporting Information).
(33) Brooks, B. R.; Bruccoleri, R. E.; Olafson, B. D.; States, D. J.; Swaminathan, S.; Karplus, M. *J. Comput. Chem.* **1983**, *4*, 187–217.
(34) (a) Kumar, D.; de Visser, S. P.; Shaik, S. *Chem.—Eur. J.* **2005**, *11*, 2825–2835. (b) de Visser, S. P.; Oh, K.; Han, A.-R.; Nam, W. *Inorg. Chem.* **2007**, *46*, 4632–4641. (c) Shaik, S.; Kumar, D.; de Visser, S. P. *J. Am. Chem. Soc.* **2008**, *130*, 10128–10140. (d) de Visser, S. P. *J. Am. Chem. Soc.* **2010**, *132*, 1087–1097.
(35) (a) Kumar, D.; de Visser, S. P.; Shaik, S. *J. Am. Chem. Soc.* **2003**, *125*, 13024–13025. (b) Kumar, D.; de Visser, S. P.; Sharma, P. K.; Cohen, S.; Shaik, S. *J. Am. Chem. Soc.* **2004**, *126*, 1907–1920. (c) de Visser, S. P. *Chem.—Eur. J.* **2006**, *12*, 8168–8177.
(36) (a) de Visser, S. P. *Chem.—Eur. J.* **2008**, *14*, 4533–4541. (b) de Visser, S. P.; Tahsini, L.; Nam, W. *Chem.—Eur. J.* **2009**, *15*, 5577–5587. (c) Porro, C. S.; Kumar, D.; de Visser, S. P. *Phys. Chem. Chem. Phys.* **2009**, *11*, 10219–10226.
(37) Becke, A. D. *J. Chem. Phys.* **1993**, *98*, 5648–5652.
(38) Lee, C.; Yang, W.; Parr, R. G. *Phys. Rev. B* **1988**, *37*, 785–789.
(39) (a) Hay, P. J.; Wadt, W. R. *J. Chem. Phys.* **1985**, *82*, 299–310. (b) Hehre, W. J.; Ditchfield, K.; Pople, J. A. *J. Chem. Phys.* **1972**, *56*, 2257–2261.
(40) (a) Wachters, A. J. H. *J. Chem. Phys.* **1970**, *52*, 1033–1036. (b) Hay, P. J. *J. Chem. Phys.* **1977**, *66*, 4377–4384. (c) Bauschlicher, C. W., Jr.; Langhoff, S. R.; Partridge, H.; Barnes, L. A. *J. Chem. Phys.* **1989**, *91*, 2399–2411. (d) Krishnan, R.; Binkley, J. S.; Seeger, R.; Pople, J. A. *J. Chem. Phys.* **1980**, *72*, 650–654.
(41) Weigend, F.; Häser, M.; Patzelt, H.; Ahlrichs, R. *Chem. Phys. Lett.* **1998**, *294*, 143–152.
(42) Becke, A. D. *Phys. Rev. A* **1988**, *38*, 3098–3100.
(43) Perdew, J. P. *Phys. Rev. B* **1986**, *33*, 8822–8824.
(44) Adamo, C.; Barone, V. *J. Chem. Phys.* **1999**, *110*, 6158–6169.
(45) (a) Handy, N. C.; Cohen, A. J. *Mol. Phys.* **2001**, *99*, 403–412. (b) Hoe, W.-M.; Cohen, A.; Handy, N. C. *Chem. Phys. Lett.* **2001**, *341*, 319–328.
(46) Perdew, J. P.; Burke, K.; Ernzerhof, M. *Phys. Rev. Lett.* **1996**, *77*, 3865–3868.
(47) Frisch, M. J. et al. *Gaussian 09*, revision A.02; Gaussian, Inc., Wallingford CT, 2009 (see the Supporting Information).
(48) Schwabe, T.; Grimme, S. *Phys. Chem. Chem. Phys.* **2007**, *9*, 3397–3406.
(49) Bakowies, D.; Thiel, W. *J. Phys. Chem.* **1996**, *100*, 10580–10594.
(50) Ahlrichs, R.; Bär, M.; Häser, M.; Horn, H.; Kölmel, C. *Chem. Phys. Lett.* **1989**, *162*, 165–169.
(51) Smith, W.; Forester, T. R. *J. Mol. Graphics* **1996**, *14*, 136–141.
(52) Sherwood, P.; et al. *J. Mol. Struct.* **2003**, *632*, 1–28 (see the Supporting Information).
(53) Billeter, S. R.; Turner, A. J.; Thiel, W. *Phys. Chem. Chem. Phys.* **2000**, *2*, 2177–2186.
(54) (a) Chottard, G.; Schappacher, M.; Ricard, L.; Weiss, R. *Inorg. Chem.* **1984**, *23*, 4557–4561. (b) Harris, D. L.; Loew, G. H. *J. Am. Chem. Soc.* **1998**, *120*, 8941–8948. (c) Shaik, S.; Kumar, D.; de Visser, S. P.; Altun, A.; Thiel, W. *Chem. Rev.* **2005**, *105*, 2279–2328.
(55) Dürr, K.; Jux, N.; Zahl, A.; van Eldik, R.; Ivanović-Burmazović, I. *Inorg. Chem.* **2010**, *49*, 11265–11260.
(56) (a) Harris, D. L.; Loew, G. H.; Waskell, L. *J. Am. Chem. Soc.* **1998**, *120*, 4308–4318. (b) Kumar, D.; Hirao, H.; de Visser, S. P.; Zheng, J.; Wang, D.; Thiel, W.; Shaik, S. *J. Phys. Chem. B* **2005**, *109*, 19946–19951. (c) Shaik, S.; Cohen, S.; Wang, Y.; Chen, H.; Kumar, D.; Thiel, W. *Chem. Rev.* **2010**, *110*, 949–1017.
(57) (a) Park, M. J.; Lee, J.; Suh, Y.; Kim, J.; Nam, W. *J. Am. Chem. Soc.* **2006**, *128*, 2630–2634. (b) Emerson, J. P.; Farquhar, E. R.; Que, L., Jr. *Angew. Chem., Int. Ed.* **2007**, *46*, 8553–8556. (c) Solomon, E. I.; Wong, S. D.; Liu, L. V.; Decker, A.; Chow, M. S. *Curr. Opin. Chem. Biol.* **2009**, *13*, 99–113.
(58) (a) Ogliaro, F.; Cohen, S.; de Visser, S. P.; Shaik, S. *J. Am. Chem. Soc.* **2000**, *122*, 12892–12893. (b) Kumar, D.; Karamzadeh, B.; Sastry, G. N.; de Visser, S. P. *J. Am. Chem. Soc.* **2010**, *132*, 7656–7667.
(59) Ghosh, A.; Taylor, P. R. *Curr. Opin. Chem. Biol.* **2003**, *7*, 113–124.
(60) (a) Siegbahn, P. E. M.; Blomberg, M. R. A.; Chen, S.-L. *J. Chem. Theor. Comput.* **2010**, *6*, 2040–2044. (b) Lonsdale, R.; Harvey, J. N.; Mulholland, A. J. *J. Phys. Chem. Lett.* **2010**, *1*, 3232–3237.
(61) (a) Shaik, S.; de Visser, S. P.; Ogliaro, F.; Schwarz, H.; Schröder, D. *Curr. Opin. Chem. Biol.* **2002**, *6*, 556–567. (b) Kumar, D.; Hirao, H.; Que, L., Jr.; Shaik, S. *J. Am. Chem. Soc.* **2005**, *127*, 8026–8027.
(62) (a) Rohde, J.-U.; In, J.-H.; Lim, M. H.; Brennessel, W. W.; Bukowski, M. R.; Stubna, A.; Münck, E.; Nam, W.; Que, L., Jr. *Science* **2003**, *299*, 1037–1039. (b) Martinho, M.; Banse, F.; Bartoli, J.-F.; Mattioli, T. A.; Battioni, P.; Horner, O.; Bourcier, S.; Girerd, J.-J. *Inorg. Chem.* **2005**, *44*, 9592–9596. (c) Sastri, C. V.; Seo, M. S.; Park, M. J.; Kim, K. M.; Nam, W. *Chem. Commun.* **2005**, 1405–1407. (d) De Oliveira, F. T.; Chanda, A.; Banerjee, D.; Shan, X.; Mondal, S.; Que, L., Jr.; Bominaar, E. L.; Münck, E.; Collins, T. J. *Science* **2007**, *315*, 835–838. (e) Jackson, T. A.; Rohde, J.-U.; Seo, M. S.; Sastri, C. V.; DeHont, R.; Stubna, A.; Ohta, T.; Kitagawa, T.; Münck, E.; Nam, W.; Que, L., Jr. *J. Am. Chem. Soc.* **2008**, *130*, 12394–12407.
(63) (a) de Visser, S. P. *J. Am. Chem. Soc.* **2006**, *128*, 15809–15818. (b) Latifi, R.; Bagherzadeh, M.; de Visser, S. P. *Chem.—Eur. J.* **2009**, *15*, 6651–6662.
(64) (a) Hirao, H.; Kumar, D.; Que, L., Jr.; Shaik, S. *J. Am. Chem. Soc.* **2006**, *128*, 8590–8606. (b) Hirao, H.; Que, L., Jr.; Nam, W.; Shaik, S. *Chem.—Eur. J.* **2008**, *14*, 1740–1756.